# Non-canonical, potassium-driven cerebrospinal fluid clearance

Huixin Xu[1,‡], Ryann M Fame[1,‡], Cameron Sadegh[1,2], Jason Sutin[3], Christopher Naranjo[4], Della Syau[4], Jin Cui[1], Frederick B Shipley[1,5], Amanda Vernon[6], Fan Gao[6,†], Yong Zhang[7], Michael J. Holtzman[7], Myriam Heiman[6], Benjamin C Warf[8], Pei-Yi Lin[3], Maria K Lehtinen[1,5 *]

[1]Department of Pathology, Boston Children's Hospital, Boston, MA 02115, USA

[2]Department of Neurosurgery, Massachusetts General Hospital and Harvard Medical School, Boston, MA 02114, USA

[3]Fetal-Neonatal Neuroimaging and Developmental Science Center, Division of Newborn Medicine, Boston Children's Hospital, Harvard Medical School, 300 Longwood Avenue, Boston, MA 02115, USA

[4]Summer Honors Undergraduate Research Program, Division of Medical Sciences, Harvard Medical School, Boston, MA 02115, USA

[5]Graduate Program in Biophysics, Harvard University, Cambridge, MA 02138, USA

[6]Broad Institute of MIT and Harvard, Cambridge, MA 02142; Picower Institute for Learning and Memory, Cambridge, MA 02139; Department of Brain and Cognitive Sciences, Massachusetts Institute of Technology, Cambridge, MA 02139, USA

[7]Pulmonary and Critical Care Medicine, Department of Medicine, Washington University, St. Louis, MO 63110, USA

[8]Department of Neurosurgery, Boston Children's Hospital, Boston, MA 02115, USA

[‡]These authors contributed equally.

[†]Current address: Bioinformatics Resource Center in the Beckman Institute at Caltech, Pasadena, CA 91125, USA

*Correspondence should be addressed to: maria.lehtinen@childrens.harvard.edu

27  **ABSTRACT**

28   Cerebrospinal fluid (CSF) provides vital support for the brain. Abnormal CSF

29   accumulation is deleterious for perinatal neurodevelopment, but how CSF leaves the brain during

30   this critical period is unknown. We found in mice a postnatal neurodevelopmental transition

31   phase featuring precipitous CSF $K^+$ clearance, accompanied by water, through the choroid plexus

32   (ChP). The period corresponds to a human fetal stage when canonical CSF clearance pathways

33   have yet to form and congenital hydrocephalus begins to manifest. Unbiased ChP metabolic and

34   ribosomal profiling highlighted this transition phase with increased ATP yield and activated

35   energy-dependent $K^+$ transporters, in particular the $Na^+$-$K^+$-$Cl^-$ and water cotransporter NKCC1.

36   ChP-targeted NKCC1 overexpression enhanced $K^+$-driven CSF clearance and enabled more

37   permissive cerebral hydrodynamics. Moreover, ventriculomegaly in an obstructive

38   hydrocephalus model was improved by ChP-targeted NKCC1 overexpression. Collectively, we

39   identified $K^+$-driven CSF clearance through ChP during a transient but critical

40   neurodevelopmental phase, with translational value for pathologic conditions.

41

44

**INTRODUCTION**

A balance between cerebrospinal fluid (CSF) production and clearance (influx/efflux) is essential for normal brain function and development (Fame and Lehtinen, 2020). Disrupted CSF volume homeostasis with excessive CSF accumulation is implicated in many pediatric brain disorders, in particular congenital hydrocephalus (Kahle et al., 2016), where patients suffer from a potentially life-threatening accumulation of CSF and frequently develop neurological deficits that last through childhood and into adult life (Vinchon et al., 2012). Schizophrenia patients can have enlarged lateral ventricles by their first episode of psychosis (Steen et al., 2006), and in some cases as early as infancy (Gilmore et al., 2010), suggesting a role for CSF clearance abnormalities in this and possibly other neurodevelopmental disorders. As another example, autism spectrum disorders are associated with altered CSF distribution patterns and enlarged CSF space surrounding the brain (Shen et al., 2017). A better understanding of developing CSF dynamics may help explain why early phases of brain development (e.g. from third trimester to 6 months after birth in human) represent a period of high vulnerability to certain congenial disorders (Volpe, 2008, Gilmore et al., 2010, Shen et al., 2017).

Critically, how CSF is cleared during this perinatal period remains a mystery. Progress in CSF dynamics research has identified several CSF clearance routes including arachnoid granulations, perineural and paravascular pathways, and meningeal lymphatics (Antila et al., 2017, Munk et al., 2019, Fame and Lehtinen, 2020). However, these systems only fully appear at later stages of life (up to 2 years in human and several weeks postnatal in mice) (Antila et al., 2017, Munk et al., 2019), and therefore are not available to contribute to CSF dynamics during these critical early phases. Identifying and manipulating the early endogenous CSF clearance mechanisms could provide one powerful approach for tackling neurodevelopmental disorders

68    involving CSF dysregulation, and may also be applied to fluid disorders affecting adults.

69        To identify how early CSF is cleared, we investigated tissues with the ability to modulate

70    CSF at this stage. The choroid plexus (ChP) is an intraventricular epithelial structure that forms

71    the majority of the blood-CSF barrier and develops prenatally. It contains diverse ion and fluid

72    transporters along its vast surface area capable of bidirectional transport (Damkier et al., 2013).

73    Although the prevailing model posits that the ChP provides net unidirectional, luminal secretion

74    of ions and water to form CSF, insufficient corroborating data have been collected under

75    physiological experimental conditions. Furthermore, historical clinical observations suggest

76    some absorptive functions of the ChP (Milhorat et al., 1970) which is supported by animal

77    studies (Oreskovic et al., 2017). Finally, broad transcriptional changes of the machinery

78    regulating fluid/ion transport support the concept of temporally dynamic and possibly context-

79    dependent ChP functions in determining net directionality of CSF transport (Liddelow et al.,

80    2013, Delpire and Gagnon, 2019).

81        To further explore potentially absorptive properties of the ChP, we studied the expression

82    of transporters, the energetic systems and ionic gradients that govern their activity, and their

83    physiological effects across the timespan of early postnatal development in mice. Taken together

84    our data support a novel role and mechanism for CSF clearance by the $Na^+$-$K^+$-$Cl^-$ and water co–

85    transporter, NKCC1, in the apical membrane of the ChP during a specific developmental period.

86    These results have implications for the pathophysiology of congenital disorders accompanied by

87    dysregulated CSF and could inform strategies for treatment of neonatal hydrocephalus and

88    perhaps other disorders.

89

## RESULTS

**CSF K$^+$ declines precipitously during a specific perinatal period**

We discovered a unique and transient phase of neurodevelopment when CSF [K$^+$] decreased rapidly. We used inductively coupled plasma optical emission spectrometry (ICP-OES) and ion chromatography (IC) to measure levels of key ions likely to govern CSF flux including Na$^+$, K$^+$, and Cl$^-$ at several developmental timepoints. CSF [K$^+$] was remarkably high at birth (9.6 ± 3.5 mM), decreased rapidly to 4.4 ± 0.9 mM by P7 (**Fig. 1A**), and later achieved adult levels of 3.1 ± 0.6 mM (**Fig. 1A**) while [Na$^+$] and [Cl$^-$] were minimally changed (**Fig. 1B**). The reduction in CSF K$^+$ was consistent with previous reports in other species (Saunders et al., 2018) and correlated with parallel changes in serum [K$^+$] such that the ratio between blood and CSF [K$^+$] remained stable (**Fig. 1C**).

Notably, K$^+$ transport has been associated with water co-transport by several K$^+$ transporters in various tissues and cell types (Zeuthen, 1994, Hamann et al., 2010, Zeuthen and Macaulay, 2012), suggesting that CSF [K$^+$] changes could drive water movement in the brain as well. Therefore, we sought to identify mechanisms underlying this fast clearance of CSF K$^+$, which may shed light on CSF outflow during this time.


**ChP metabolism increases during the early postnatal transition phase**

We found that the transitional period of rapid CSF K$^+$ clearance coincided with high ChP metabolism. We reasoned that K$^+$ clearance during this period could be ChP-mediated because the ChP expresses high levels of K$^+$ co-transporters on its large CSF-contacting surface area (Keep and Jones, 1990, Damkier et al., 2013). Similar to water and ion transport by other epithelial structures such as kidney proximal and distal tubes (Bhargava and Schnellmann, 2017),

113    $K^+$ clearance from CSF by the ChP would be energy-dependent and therefore be accompanied by

114    upregulation of ATP production and mitochondrial activity. Therefore, we evaluated the

115    metabolic status and ATP production capacity of the ChP epithelium before, during, and after the

116    time period of CSF $[K^+]$ reduction. We found that both mitochondria number and size increased

117    from E16.5 to 2mo (**Fig. 1D-G**), while cellular glycogen load gradually decreased

118    (**Supplementary Fig. 1**). Both observations are consistent with reports from ChP in other

119    mammalian species (Netsky and Shuangshoti, 1975, Keep and Jones, 1990) and suggest

120    functional changes in ChP oxidative metabolism. To assess this we monitored oxygen

121    consumption to calculate basal metabolism and ATP production at embryonic day 16.5 (E16.5),

122    postnatal day 0 (P0), P7, and adult (2 months old (2mo)) ChP explants using Agilent Seahorse

123    XFe technology (**Fig. 1H, Supplementary Fig. 2**). We found that E16.5 ChP had the lowest

124    basal respiration of all tested ages (**Fig. 1I, Supplementary Fig. 2**). Adult had a higher capacity

125    for overall ATP production than E16.5 ChP, but surprisingly, P0-P7 ChP were the most

126    metabolically active as per ATP production (**Fig. 1I, J**). In addition, mitochondrial subcellular

127    distribution in ChP epithelium was biased toward the apical surface as postnatal development

128    proceeded, with E16.5 mitochondria heavily distributed along the basal side of epithelial cells,

129    P0 mitochondria intermediately localized, and P7 and 2mo mitochondria having more apical

130    distribution (**Fig. 1K-M, Supplementary Fig. 3**). Mitochondrial subcellular localization

131    responds to regional energy demand in other cellular processes such as migration of mouse

132    embryonic fibroblasts and during axonal outgrowth (Schuler et al., 2017, Smith and Gallo, 2018).

133    Together with the increase in ATP production postnatally, the shift in ChP epithelial

134    mitochondria distribution over postnatal development suggests increasing ATP supply to meet

135    high demand at the apical ChP surface during the early postnatal phase, concurrent with the rapid

136    clearance of CSF $K^+$. This concurrence prompted us to investigate energy-dependent

137    mechanisms whereby ChP epithelial cells might contribute to $K^+$ clearance.

**138    The ChP increases production of CSF-facing ion and water transporters postnatally**

139        Consistent with rapid CSF $K^+$ clearance and high ChP metabolism, we found that

140    expression of the energy-dependent cation transport pathway components were upregulated in

141    ChP postnatally. To unbiasedly identify candidates controlling postnatal CSF clearance through

142    the ChP, we conducted ribosomal profiling to investigate transcripts that are prioritized for

143    translation in embryonic (E16.5) and adult (2 mo) ChP, using Translating Ribosomal Affinity

144    Purification (TRAP; Heiman et al., 2008). ChP epithelial cells were targeted by crossing

145    *FoxJ1:cre* mice (Zhang et al., 2007) with *TRAP* (*EGFP:L10a*) mice (Heiman et al., 2008) (**Fig.**

146    **2A, Supplementary Fig. 4A, B**), and mRNA associated with the L10a ribosomal subunit were

147    purified for sequencing.

148        TRAP analyses revealed 1967 differentially translated transcripts (adjusted $p < 0.05$)

149    between E16.5 and 2mo adult ChP: 1119 enriched at E16.5 and 847 enriched at 2mo (**Fig. 2B**).

150    Gene set and pathway analyses revealed developmentally regulated ChP programs. Adult (2mo)

151    ChP had enriched functional gene sets associated with active transmembrane membrane

152    transport and mitochondria, which is consistent with our abovementioned findings on

153    metabolism changes (**Fig. 2C**). Specifically, cation transport was enriched, supporting the

154    hypothesis of ChP mediating CSF $K^+$ transport postnatally (**Fig. 2C, D**). Enriched pathways in

155    the 2mo adult included secretion associated pathways named for other, better studied secretory

156    processes, including salivary and pancreatic secretion, all of which have a special emphasis on

157    water and ion transmembrane transport (**Supplementary Fig. 4C (red), D**). Consistent with a

158    rise in fluid and ion modulating machinery, there was a striking enrichment of more

159    transmembrane and signal peptide-containing transcripts in adult ChP (**Supplementary Fig. 4E,**

160    **F**). These results indicate that the ChP specifically gained fluid and ion modulatory functions

161    postnatally.

162

163    **NKCC1 is poised to mediate perinatal ChP CSF K$^+$ and water clearance**

164            Among all fluid and ion modulating candidates with increasing postnatal expression

165    (**Supplementary Fig. 4G, H**), we identified NKCC1 (*Slc12a2*) as the candidate most likely to

166    mediate CSF clearance. NKCC1 is functionally related to Na$^+$/K$^+$-ATPase (*Atp1a1* and *Atp1b1*),

167    as the latter actively maintains the Na$^+$/K$^+$ gradient that powers NKCC1. Both Na$^+$/K$^+$-ATPase

168    and NKCC1 are capable of CSF K$^+$ clearance, but NKCC1 was of particular interest because (1)

169    it is a co-transporter of K$^+$ and water (Zeuthen and Macaulay, 2012, Steffensen et al., 2018); and

170    (2) the activity of NKCC1 can be further modified by phosphorylation (Darman and Forbush,

171    2002), lending additional control to its fluid/ion modulatory capacity. In addition, NKCC1 is

172    particularly enriched in the ChP and does not impact broad functionality like the Na$^+$/K$^+$-ATPase

173    does, both of which are ideal features for a functional therapeutic intervention target. We refined

174    our temporal expression analyses of NKCC1, ATP1a1, ATP1b1, and Klotho (*Kl*), which

175    contributes to the membrane localization of the Na$^+$/K$^+$-ATPase (Razzaque, 2008, Sopjani et al.,

176    2011) (**Fig. 2E**), by sampling weekly from P0 to P28 and then at 2mo and confirmed increased

177    expression of transcript and protein for each component across developmental time (**Fig. 2F, G,**

178    **Supplementary Fig. 5**). The observed changes in NKCC1 total protein were corroborated by an

179    independent approach where the rate of ChP epithelial cell swelling under high [K$^+$] challenge

180    (Steffensen et al., 2018) reflected the abundance of NKCC1 protein (**Fig. 2H-J, Supplementary**

181    **Fig. 6**).

182        In addition, we found particularly high levels of phosphorylated, therefore activated

183        (Darman and Forbush, 2002), NKCC1 (pNKCC1) in the ChP of P0-P7 pups, with P7 having

184        peak pNKCC1 levels among all postnatal ages, indicative of increased NKCC1 activity during

185        the first postnatal week (**Fig. 2G**). Similar to the timeline of ChP ATP production (**Fig. 1J**), the

186        timeframe of high ChP pNKCC1 was concurrent with the fast CSF $[K^+]$ decrease during the first

187        postnatal week (**Fig. 1A**), suggesting a functional correlation and further confirming the

188        significance of the early postnatal transitional period. Taken together, we identified ChP NKCC1

189        as the top candidate for mediating postnatal CSF $K^+$ and water clearance.

190

191        **NKCC1 temporal regulation requires epigenetic control that is implicated in congenital**

192        **hydrocephalus**

193        We found that the temporal profile of NKCC1 expression was tightly regulated at the

194        epigenetic level by modulators implicated in some forms of congenital hydrocephalus. The

195        NuRD complex governs differentiation and maturation of diverse cells and tissues (Goodman

196        and Bonni, 2019). Our previously published RNA sequencing studies (Lun et al., 2015)

197        identified NuRD components, including the ATPase CHD family members (Chd4 being the most

198        highly expressed), the histone deacetylases HDAC1/2, and methyl CpG-binding domain protein

199        MBD3 in the ChP (**Fig. 3A**). *De novo* loss-of-function CHD4 mutations are implicated in some

200        groups of children with congenital hydrocephalus and ventriculomegaly (Weiss et al., 2020). We

201        found that CHD4 localized to nuclei in mouse ChP epithelial cells beginning at P0 (**Fig. 3B**).

202        Immunoprecipitation of CHD4 identified HDAC1, HDAC2, and MBD3 by immunoblotting in

203        mouse ChP (**Fig. 3C,** technical control for Co-IP protocol is shown in **Supplementary Fig. 7**),

204        confirming the existence of the CHD4/NuRD complex in developing ChP. We then disrupted the

205   complex by generating ChP-*Chd4* deficient mice. Cre was expressed in *Chd4* floxed mice (*Chd4*

206   fl/fl) (Williams et al., 2004) using an adeno-associated viral vector (AAV) with tropism for the

207   ChP (AAV2/5) (Haddad et al., 2013), delivered by *in utero* intracerebroventricular (ICV)

208   injection at E14.5. *Chd4* transcript levels dropped to <50% by P7 (**Fig. 3D**). While CHD4

209   protein levels only substantially decreased by P14 (**Fig. 3E, G**), we found that the developmental

210   increase of ChP NKCC1 expression was disrupted as soon as the CHD4 protein decreased and

211   lasted at least until P28 (**Fig. 3F, G**). Similar results were also observed in 4VChP (**Fig. 3H, I**).

212   The expression of other developmentally regulated, functionally relevant candidates (*atp1a1,*

213   *atp1b1, and klotho*) was not affected (data not shown). These data confirm that the NuRD/ChD4

214   complex is one of the required components tightly regulating ChP NKCC1 developmental

215   expression.

216

217   **ChP NKCC1 actively mediates CSF clearance during the early postnatal transition phase**

218         To test whether NKCC1 is indeed capable of transporting from CSF into the ChP during

219   the period of rapid CSF [K$^+$] decline, we induced NKCC1 overexpression (OE) in developing

220   ChP epithelial cells using AAV2/5. NKCC1 transport directionality follows combined Na$^+$, K$^+$,

221   Cl$^-$ gradients, which are close to being neutral in adult brains and likely to bias towards the CSF-

222   to-ChP direction during the early postnatal phase. NKCC1 protein level would be rate-limiting

223   during the early postnatal time when it is already highly phosphorylated, unlike in older mice

224   where pNKCC1 only represented a small portion of total NKCC1. The goal of this OE approach

225   was to accelerate endogenous ChP NKCC1 transport, thereby revealing its directionality based

226   on whether CSF [K$^+$] clearance was enhanced or delayed.  AAV2/5-NKCC1, which expresses

227   NKCC1 fused to an HA tag (Somasekharan et al., 2013), or control GFP virus was delivered by

228    *in utero* ICV at E14.5. Successful NKCC1 OE and increased pNKCC1 was confirmed in ChP at

229    P0 (**Fig. 4A-D**). Appropriate localization to apical membranes of epithelial cells, transduction

230    efficiency, and tissue specificity were also validated (**Fig. 4E-I, Supplementary Fig. 8 A, B**).

231    Transcript levels of other $K^+$ transporters or channels did not change following AAV2/5-NKCC1

232    transduction (**Supplementary Fig. 8C**). Because CSF $[K^+]$ sharply decreased from P0 to P7 (**Fig.**

233    **1A**), we sampled CSF from ChP NKCC1 OE and control mice at P1. We found that ChP

234    NKCC1 OE reduced CSF $[K^+]$ more than controls, with their P1 CSF $[K^+]$ values closely

235    approximating those normally observed at P7 (**Fig. 4J**), indicating accelerated $K^+$ clearance from

236    CSF after enhanced ChP NKCC1 activity. CSF total protein levels were not affected (AAV2/5-

237    GFP = $2.50 \pm 0.20$ mg/ml vs. AAV2/5-NKCC1 = $2.71 \pm 0.46$ mg/ml; N = 6 from two litters each;

238    $p = 0.34$, unpaired t-test). Overall, these findings support a model in which, under physiological

239    conditions with high early postnatal CSF $[K^+]$, ChP NKCC1 transports $K^+$ out of CSF.

240         Next, we found that the circulating CSF volume in ChP NKCC1 OE mice was reduced,

241    as reflected by smaller lateral ventricles. To avoid any tissue processing artifacts, we conducted

242    live T2-weighted magnetic resonance imaging (MRI) (**Fig. 5A**) to quantify lateral ventricle

243    volume. AAV-GFP mice were indistinguishable from naive wild-type mice at P14. In contrast,

244    NKCC1 OE mice had reduced lateral ventricle volumes (**Fig. 5A, B**), without decrease in overall

245    brain size (**Fig. 5C**), reflecting less circulating CSF. The difference in ventricle sizes from these

246    same mice was sustained up to our final measurement at P50 (AAV-GFP: $3.12 \pm 0.59$ mm$^3$ vs.

247    AAV-NKCC1: $1.28 \pm 0.28$ mm$^3$, * $p = 0.0182$). While the exact transport direction of NKCC1 in

248    adult ChP is still under debate (Delpire and Gagnon, 2019), the consistency in ventricular

249    volume from P14 into later life supports our working model that because a relatively small

250    proportion of ChP NKCC1 was phosphorylated in mice P14 and older (**Fig. 2G**), NKCC1 levels

251    are not rate-limiting and thus OE would not as substantially impact ChP functions in older

252    animals. Collectively, our findings demonstrate that ChP NKCC1 mediated CSF clearance

253    during the first postnatal week. Augmenting this process impacted CSF volume homeostasis in

254    the long term.

255        We then tested and found that enhancing CSF clearance through ChP NKCC1 OE

256    changed how the brain and cranial space adapted to CSF volume changes. Intracranial

257    compliance ($C_i$) and CSF resistance ($R_{CSF}$) describe the ability of the entire intracranial space

258    (including brain, meninges, and outflow routes) to accommodate an increasing CSF volume that

259    would otherwise increase intracranial pressure (ICP). In humans, these parameters are measured

260    by a CSF constant rate infusion test (Aquilina et al., 2012, Eide, 2018, Lalou et al., 2018) and

261    can aid in diagnosis and evaluation of conditions like hydrocephalus, which has decreased $C_i$

262    (Kahle et al., 2016). We developed a miniaturized version of this test to determine the $C_i$ and

263    $R_{CSF}$ in mice. The constant rate infusion test artificially increases CSF volume by ICV infusion

264    of artificial CSF (aCSF), causing ICP to rise and plateau at a new level (**Fig. 5D, E**). The $C_i$ and

265    $R_{CSF}$ are estimated from the ICP vs. time curve using Marmarou's model of CSF dynamics

266    (Czosnyka et al., 2012) (**Supplementary Fig. 9A**). Simply put, the $C_i$ is proportional to the rate

267    of ICP increase, and the $R_{CSF}$ is related to the level of the post-infusion ICP plateau (**Fig. 5E**). As

268    a quality control for the correct placement of infusion and measurement catheter, arterial and

269    respiratory pulsations were clearly visible in the ICP waveform and their amplitude increased

270    with volume load as expected (**Supplementary Fig. 9B, C**). Using this approach, we found that

271    ChP NKCC1 OE significantly increased $C_i$ at an age of 5-7 weeks (**Fig. 5F, G**), consistent with

272    the brain having greater capacity for CSF in ventricles "deflated" due to excessive CSF clearance.

273    Resting ICP and $R_{CSF}$ were unchanged (**Fig. 5H, I**).

274

**Enhanced ChP NKCC1 function mitigates ventriculomegaly in a model of obstructive**

**hydrocephalus**

277       Our findings of enhanced CSF clearance after ChP NKCC1 OE indicate that ChP

278 NKCC1 can remove excess CSF. Therefore, we hypothesized that ChP NKCC1 OE expression

279 could mitigate ventriculomegaly in a model of postnatal obstructive hydrocephalus. We first

280 overexpressed ChP NKCC1 at E14.5 by in utero AAV2/5 ICV, then introduced obstructive

281 hydrocephalus by a single unilateral injecting of kaolin into the lateral ventricle at P4 (Shaolin et

282 al., 2015), and finally evaluated the lateral ventricle volumes by live T2 MRI at P14 (**Fig. 6A**).

283 While both NKCC1 OE and control mice had enlarged ventricles at P14, NKCC1 OE mice had

284 reduced ventriculomegaly compared to controls, with the average ventricle volume being less

285 than 1/3 of the controls (**Fig. 6B-D;** ventricles marked by blue arrows; kaolin deposits marked by

286 red arrows). Taken together, our findings demonstrate that early, ChP targeted NKCC1 OE has a

287 sustained and broad impact on specific volumetric and biophysical parameters of the intracranial

288 space with potential therapeutic applications to hydrocephalus.

289

290 **DISCUSSION**

291    In this study we sought to understand how CSF is cleared from the brain before the

292 development of canonical CSF outflow routes (e.g. arachnoid granulations and meningeal

293 lymphatics) (Antila et al., 2017, Munk et al., 2019). The intervening time period is a critical,

294 transient phase in brain development when failure of CSF clearance has debilitating

295 consequences (Volpe, 2008). Our results suggest that this period is defined by rapid decrease in

296 CSF $K^+$. The ChP mediates the CSF $K^+$ clearance during this transition period, and thus forms a

297 CSF outflow route through ion and water co-transport by NKCC1 (**Fig. 7**). This CSF clearance

298 by the ChP contrasts the prevailing models that ChP constantly, unidirectionally secretes CSF.

299 Taken together, we discovered an unconventional, precisely timed, function of the developing

300 ChP that clears CSF prior to the formation of other canonical routes, and provides targets for

301 fluid management intervention during a critical transition phase of brain development.

302    NKCC1 is a bidirectional transporter, recently discovered to be an important co-

303 transporter of water in the adult ChP (Steffensen et al., 2018). Although clearly established as a

304 key molecular mechanism of CSF regulation, ChP NKCC1 transport direction and its

305 determinants *in vivo* have been actively debated due to the technical challenges of 1) specifically

306 manipulating ChP NKCC1 without affecting NKCC1 in other CSF-contacting cells, instead of

307 ICV application of chemicals such as NKCC1 inhibitor bumetanide; and 2) accurately

308 determining intracellular ion levels of ChP epithelial cells, and therefore ion gradients, under

309 physiological conditions, as summarized in **Supplementary Table 1** and reviewed by Delpire

310 and Gagnon (Delpire and Gagnon, 2019). Our *in vivo* "gain-of-function" approach effectively

311 bypasses the abovementioned technical limitations. By overexpressing NKCC1 specifically in

312 the ChP through AAV transduction to amplify its physiological functional impact, we could

313    subsequently observe the resulting CSF $K^+$ and fluid volume changes to reveal the transporter's

314    native directionality. Using this approach, we found that, in contrast to the common notion that

315    the ChP constantly produces CSF, NKCC1 in the ChP mediated CSF clearance when CSF $[K^+]$

316    is above adult values, especially during the first postnatal week in mice. This phase corresponds

317    to the third trimester to 6 months after birth in human, which represents a window of high

318    vulnerability to congenial fluid disorders (Volpe, 2008).

319        We next demonstrated that the ChP clearance of CSF can be targeted to temper abnormal

320    CSF accumulation. The ChP has been targeted for therapeutic manipulation in rodent models of

321    neurologic diseases ranging from Huntington's disease and lysosomal storage disorders, to

322    Alzheimer's disease, where transduction of exogenous gene products into ependymal or ChP

323    epithelial cells has improved cardinal symptoms of disease (Kaler, 1994, Hudry et al., 2013).

324    Encouragingly, we showed that enhancing ChP epithelial cell NKCC1 transport capacity

325    lessened the severity of ventriculomegaly in a model of obstructive hydrocephalus. Our data

326    demonstrate the possibility of tempering congenital hydrocephalus by augmenting endogenous

327    ChP NKCC1 activity to increase CSF absorption rates during early development when CSF $[K^+]$

328    is high. In addition, because ChP CSF absorption via NKCC1 is driven by increased CSF $[K^+]$,

329    this mechanism may come into play in other pathogenic conditions where CSF $[K^+]$ is transiently

330    increased, such as after tissue injury or ventricular bleeding. Therefore, our findings emphasize

331    the ChP as a targetable, $K^+$-sensitive and on-demand CSF drainage route in neurological

332    disorders where CSF homeostasis is disrupted.

333        Further, in light of recent findings reporting hydrocephalus and ventriculomegaly in

334    children with *de novo* loss-of-function CHD4 mutations (Weiss et al., 2020), we found that the

335    CHD4/NuRD complex is required for the developmental regulation of NKCC1 expression. This

336    connection suggests a possible pathophysiological mechanism whereby lack of CHD4 activity

337    might reduce NKCC1 levels during early development (equivalent to P0-P7 in mice), and lead to

338    insufficient CSF clearance resulting in hydrocephalus. In our loxP-cre approach, most CHD4

339    protein knockdown and resulting stagnation of NKCC1 expression occurred by P14, which is

340    beyond the critical window of NKCC1 activity at P0-P7. As such, we did not model

341    developmental ventriculomegaly with this approach. Improved genetic tools for early CHD4

342    knockout and new animal models harboring the *de novo* patient mutations would be required to

343    fully unravel the regulatory connection between CHD4/NuRD complex and NKCC1.

344    A key question that emerges from this work is: If the ChP is acting as an outflow

345    pathway rather than a source of CSF during this transitional developmental phase – where does

346    the early CSF water content come from? One mechanism that could be acting at this stage is CSF

347    secretion by the developing brain tissue (e.g. progenitor cells that have a cell body at the

348    ventricular zone but extend their basal processes to the developing pia) which secretes CSF

349    immediately after neural tube closure (Gato et al., 2014). Future studies should elucidate whether

350    this mechanism extends into this transitional phase. Consistent with progenitor involvement in

351    CSF dynamics, recent identification of genes driving pediatric hydrocephalus shows affected

352    genes to be expressed predominantly by cortical progenitor cells lining the brain's ventricles

353    (Furey et al., 2018), and not the ChP, suggesting a non-choroidal source of CSF as an alternative

354    contributor to abnormal CSF production.

355    In addition to fluid regulation, the newly identified ChP clearance route provides a key

356    mechanism to regulate extracellular $K^+$ during the first postnatal week. The subunits of the major

357    system for moving $K^+$ against its individual concentration gradient, the $Na^+/K^+$-ATPase (i.e.

358    Atp1a1 and Atp1b1), were not yet at their full expression levels during this period. The ChP

359 NKCC1-mediated $K^+$ clearance mechanism might assist in establishing the $K^+$ gradient in a

360 timely manner, which is crucial for cellular physiology (Rasmussen et al., 2020). Notably, the

361 period of rapidly decreasing CSF $[K^+]$ overlaps with the developmental phase when the

362 excitatory-to-inhibitory "GABA switch" occurs. In early cortical progenitor cells that reside in

363 the ventricular zone and are bathed by CSF, the classic inhibitory neurotransmitter GABA leads

364 to excitatory potentials and suppression of DNA synthesis (LoTurco et al., 1995). As newborn

365 cortical neurons differentiate and migrate away from the ventricular zone, GABA switches to

366 adopt the more classic role as an inhibitory neurotransmitter by lowering intracellular $Cl^-$ (Owens

367 et al., 1999) which is achieved through coordinated activities of neuronal $K^+/Cl^-$ co-transporters

368 KCC2 and NKCC1 (Pisella et al., 2019, Watanabe et al., 2019). Because ions, including $K^+$, can

369 traffic from CSF into interstitial fluid (Cserr, 1965, Fencl et al., 1966), any interference with the

370 developmental timeline of ChP NKCC1 that resulted in delayed CSF $K^+$ clearance could

371 potentially increase extracellular/interstitial fluid $[K^+]$ and affect neural physiology (Rasmussen

372 et al., 2020). Specifically, such a change in extracellular/interstitial fluid $[K^+]$ could

373 fundamentally impact neuronal NKCC1 and KCC2 transport equilibrium, potentially

374 contributing to a delayed GABA switch, a phenomenon reported in many models of

375 neurodevelopmental and psychiatric disorders including subtypes of autism spectrum disorder

376 (Amin et al., 2017), Rett syndrome (Banerjee et al., 2016), Fragile X syndrome (He et al., 2014),

377 schizophrenia (Hyde et al., 2011), and Down syndrome (Deidda et al., 2015). Furthermore,

378 extracellular $[K^+]$ and certain $K^+$ channels also regulate activities of microglia (Madry et al.,

379 2018), which are critical in synaptic pruning during postnatal neurodevelopment in mice

380 (Schafer et al., 2012). Thus, the ChP is poised to play important roles in proper CNS formation

381 by creating and maintaining desirable extracellular ionic homeostasis at different developmental

382    stages, with subsequent effects on neuronal maturation, circuit formation, and

383    neuroinflammatory homeostasis.

384          Beyond key findings and implications during this critical transitional developmental stage,

385    our study introduced a murine ICP measurement device combined with constant CSF infusion.

386    This approach provides a much-needed advance in fluid research technology that can be broadly

387    applied to study essentially all CSF dynamic systems across the mouse lifespan. We adapted our

388    tool from clinical practice to provide a range of options for measuring global cerebral fluid states

389    that reflect the interaction between CSF and cranial tissues. In later life, CSF homeostasis is

390    maintained by collaborative efforts from multiple players in the brain, including the ChP, the

391    dural lymphatics (Antila et al., 2017), glymphatics (Munk et al., 2019), leptomeningeal

392    vasculature (Li et al., 2020), and the ependyma (Spassky et al., 2005). While this approach

393    measures overall cranial fluid dynamics as one single unit, future applications could apply

394    mathematical models that have been proposed to isolate the contribution of distinct CSF outflow

395    routes using data acquired from human patients (Vinje et al., 2020). Such adaptability secures the

396    broadening relevance of our tool and inspires optimism for further improved resolution in

397    studying brain fluid dynamics. Availability of this new tool also allows future researchers to

398    obtain measurements in support of the growing comprehensive "systems" view of regulatory

399    mechanisms of CSF-brain interactions.

400          In summary, our study presents a critical transient phase when the ChP acts as a non-

401    canonical route for CSF clearance prior to the maturation of other canonical clearance pathways.

402    ChP NKCC1 mediates CSF clearance in a $K^+$-dependent manner. Targeting this absorption route

403    holds promise in improving fluid management for congenital hydrocephalus and other CSF

404    disorders.

405 **ACKNOWLEDGEMENTS**

421

422 **Author contributions:** H.X., R.M.F., C.S. J.S., P.-Y. L., B.C.W., F.B.S., J.C., D.S., C.N., and

423 M.K.L. designed and performed experiments; H.X., R.M.F., C.S., and J.S. analyzed the data;

424 Y.Z. and M.J.H. provided material; A.V., F.G., and M.H. provided technological support; H.X.,

425 R.M.F., and M.K.L. wrote the manuscript. All co-authors edited the manuscript.

426

427 **Declaration of interests:** The authors declare that no competing interests exist.

428 **METHODS**

429 Mice

430  The Boston Children's Hospital IACUC approved all experiments involving mice in this

431 study. Timed pregnant CD1 dams were obtained from Charles River Laboratories. Mice with

432 germline loxP-CHD4-loxP were imported from MGH and bred in-house. Both male and female

433 mice were equally included in the study and were analyzed at postnatal day 0, 7, 14, 21, 28, 5-

434 7weeks, and 2+ months. Animals were housed in a temperature-controlled room on a 12-hr

435 light/12-hr dark cycle and had free access to food and water. For studies involving mice younger

436 than postnatal day 10, all mice were allocated into groups based solely on the gestational age

437 without respect to sex (both males and females were included). For studies involving mice older

438 than 10 days, both male and female are included intentionally.

439 CSF Collection and Metal Detection

440  CSF was collected by from cisterna magna using a glass capillary, and collected CSF was

441 centrifuged at 10,000xg for 10min at 4℃ to remove any tissue debris. Metal quantifications were

442 performed by Galbraith Laboratories, Inc. (Knoxville, TN, USA). Inductively coupled plasma -

443 optical emission spectrometry (ICP-OES) was used for K and Na quantification, and ion

444 chromatography (IC) was used for the Cl⁻ quantification. All tests were performed using 5-7μL

445 of CSF.

446 TRAP

447  Mice aged 8 weeks or E16.5 from the *Foxj1*:Cre x EGFP-L10a Bacterial Artificial

448 Chromosome (BAC) transgenic lines (N=3, each N included LVChP pooled from 3 mice) were

449 used and brain tissue was immediately dissected and used for TRAP RNA purifications as

450   previously described (Heiman et al., 2008). RNA quality was assessed using Bioanalyzer Pico

451   Chips (Agilent, 5067-1513) and quantified using Quant-iT RiboGreen RNA assay kit (Thermo

452   Fisher Scientific R11490). Libraries were prepared using Clonetech SMARTer Pico with

453   ribodepletion and Illumina HiSeq to 50NT single end reads. Sequencing was performed at the

454   MIT BioMicroCenter.

455   Sequencing Data Analysis

456        The raw fastq data of 50-bp single-end sequencing reads were aligned to the mouse

457   mm10 reference genome using STAR 2.4.0 RNA-Seq aligner (Dobin et al., 2013). The mapped

458   reads were processed by htseq-count of HTSeq software (Anders et al., 2015) with mm10 gene

459   annotation to count the number of reads mapped to each gene. The Cuffquant module of the

460   Cufflinks software (Trapnell et al., 2010) was used to calculate gene FPKM (Fragments Per

461   Kilobase of transcript per Million mapped reads) values. Gene differential expression test

462   between different animal groups was performed using DESeq2 package (Love et al., 2014)

463   with the assumption of negative binomial distribution for RNA-Seq data. Genes with adjusted p-

464   value< 0.05 are chosen as differentially expressed genes. All analyses were performed using

465   genes with FPKM> 1, which we considered as the threshold of expression (Figure 2- source

466   data).

467   Sequencing Pathway and Motif Analysis

468        Functional annotation clustering was performed using DAVID v6.7 (Huang da et al.,

469   2009). Gene ontology (GO) analysis was performed using AdvaitaBio iPathway guide V.v1702.

470   Enrichment vs. perturbation analysis was performed by AdvaitaBio iPathway guide V.v1702 and

471   allows comparison of pathway output perturbation and cumulative gene set expression changes.

472   In brief, the enrichment analysis is a straightforward gene-set enrichment over representation

473    analysis (ORA) considering the number of differentially expressed genes (DEGs) that are

474    assigned to a given pathway. The enrichment value is expressed as a proportion of enriched

475    members to total genes in a defined pathway and a p-value (Fisher) is calculated for this score,

476    however false positives have been reported at up to 10% with this method (Draghici et al., 2007).

477    Perturbation, on the other hand, uses pathway data that applies relationships between gene

478    products rather than only using a list. Perturbation assigns an impact score based on a

479    mathematical model that captures the entire topology of the pathway and uses it to calculate how

480    changes in the expression of each gene in the pathway would perturb the absolute output of the

481    pathway (Draghici et al., 2007). Then, these gene perturbations are combined into a total

482    perturbation for the entire pathway and a p-value is calculated by comparing the observed value

483    with what is expected by chance. Motif analyses were performed using SignalP (v5.0; Almagro

484    Armenteros et al., 2019) and TMHMM (v2.0; Sonnhammer et al., 1998).

485    Transmission Electron Microscopy

486        All tissue processing, sectioning, and imaging was carried out at the Conventional

487    Electron Microscopy Facility at Harvard Medical School. Forebrain tissues were fixed in 2.5%

488    Glutaraldehyde/2% Paraformaldehyde in 0.1 M sodium cacodylate buffer (pH 7.4). They were

489    then washed in 0.1M cacodylate buffer and postfixed with 1% Osmiumtetroxide (OsO4)/1.5%

490    Potassiumferrocyanide (KFeCN$_6$) for one hour, washed in water three times and incubated in 1%

491    aqueous uranyl acetate for one hour. This was followed by two washes in water and subsequent

492    dehydration in grades of alcohol (10 minutes each; 50%, 70%, 90%, 2x10min 100%). Samples

493    were then incubated in propyleneoxide for one hour and infiltrated overnight in a 1:1 mixture of

494    propyleneoxide and TAAB Epon (Marivac Canada Inc. St. Laurent, Canada). The following day,

495    the samples were embedded in TAAB Epon and polymerized at 60 degrees C for 48 hours.

496 Ultrathin sections (about 80nm) were cut on a Reichert Ultracut-S microtome, and picked up

497 onto copper grids stained with lead citrate. Sections were examined in a JEOL 1200EX

498 Transmission electron microscope or a TecnaiG² Spirit BioTWIN. Images were recorded with an

499 AMT 2k CCD camera.

500 Glycogen and Mitochondrial Quantification

501 Glycogen and mitochondrial quantification was performed by hand using the ImageJ

502 plugin FIJI (Schindelin et al., 2012, Schneider et al., 2012). Percentages were calculated by

503 dividing the area of interest by the total area of ChP epithelial cell within the field of view. No

504 other cell types were included in the analysis. For each condition, analyses were performed

505 across multiple individual animals (N=3 for each age). From each animal, 10-20 fields of view

506 were imaged at 3,000x for glycogen analysis and 5-10 fields of view were imaged at 3,000x for

507 mitochondrial analysis. Each different field of view represented a unique cell or cells, and fields

508 of view were chosen such that both the apical and basal surfaces of the cell were visible. For

509 mitochondrial distribution, a custom MatLab (v.2018) code was written to extract the centroid

510 from mitochondria data traced in ImageJ ROIs (Supplementary file). Then a distance

511 transformation was performed from each mitochondrion centroid to the hand-traced apical or

512 basal surfaces. The shortest distance was extracted to calculate the apical: basal proximity ratio,

513 such that 1= on the apical surface and 0= on the basal surface. The analyses included a total of

514 1747 adult mitochondria, 2241 P7 mitochondria, 2257 P0 mitochondria, and 1123 embryonic

515 mitochondria.

516 Seahorse Metabolic Analysis

517 ChP explants were dissected in HBSS (Fisher, SH30031FS) and maintained on wet ice

518    until plated. Only the posterior leaflet of the P0, P7, and adult ChP was retained for analysis due

519    to empirically determined limitations of the oxygen availability in the XFe96 Agilent Seahorse

520    system. Tissue explants were plated on Seahorse XFe96 spheroid microplates (Agilent, 102905-

521    100) coated with Cell TAK (Corning), in Seahorse XF Base Medium (Agilent, 102353-100)

522    supplemented with 0.18% glucose, 1mM L-glutamine, and 1mM pyruvate at pH7.4 and

523    incubated for 1 hour at 37 °C in a non-$CO_2$ incubator. Extracellular acidification rates (ECAR)

524    and oxygen consumption rates (OCR) were measured via the Cell Mito Stress Test (Agilent,

525    103015-100) with a Seahorse XFe96Analyzer (Agilent) following the manufacturer's protocols.

526    Data were processed using Wave software (Agilent). ATP production was calculated as the

527    difference in OCR measurements before and after oligomycin injection, as described by the

528    manufacturer's protocol (Agilent, 103015-100). The Cell Mito Stress test was performed 2-5

529    independent times. The individual analyses were performed by averaging the readings from both

530    the right and left hemisphere lateral ventricle ChP for each individual. Data were normalized by

531    Calcein-AM (2μM in PBS, Life Technologies L-3224) fluorescence measured at the end of the

532    assay. Data are presented normalized to the adult levels for each assay to account for any

533    experimental variability.

534    High K$^+$ challenge study

535    Fresh LV ChPs were collected from P4 pups and adult mice in room temperature HBSS

536    and glued down onto imaging dishes with coverslip bottom. The tissues were incubated at 37 °C

537    with Calcein-AM (Invitrogen L3224; 1:200) for 10min and then rinsed with 37 °C artificial CSF

538    (aCSF: 119 mM NaCl, 2.5 mM KCl, 26 mM $NaHCO_3$, 1 mM $NaH_2PO_4$, 11 mM glucose, with

539    fresh 2.0 mM magnesium chloride and 2.8 mM calcium chloride). The tissues were soaked in

540    1.8ml aCSF at the beginning of each imaging session and allowed to stabilize for 10min. One Z-

541    stack was acquired to reflect the baseline cell volume. Then a 10x KCl solution in aCSF was

542    spiked into the bath to make the final bath $K^+$ concentration 50mM immediately before imaging

543    subsequent continued. A total of five 3D Z-stacks were acquired throughout a 10-min imaging

544    session to capture changes in cellular volume over time. Each stack took less than 30s to

545    minimize changes in cell volume from the beginning to the end of each stack. All imaging

546    studies were carried out at 37°C. Image stacks were imported into Imaris (Bitplane) software.

547    Individual epithelial cells were identified by shape. Cells with discrete borders that were present

548    at all timepoints and had dark pixels both above and below them in Z for the whole timecourse

549    were selected *a priori* and then traced by hand using the "Surpass" functionality to create a 3D

550    surface volume through all Z stacks based on Calcein-AM uptake signal. Due to known z-step

551    distance and interpolation between the planes, Imaris calculated the number of voxels for each

552    cell. This analysis was then repeated for the same cell throughout the timecourse. We verified

553    manually that the cell was the same individual based on the topology of the surrounding cells,

554    allowing for adjustment for any x-y drifting that occurred. The relative volume was calculated as

555    $dV/V_0$ for each timepoint (t) where $V_0$ is the initial volume of the cell, t is each subsequent

556    timepoint after addition of challenge, and $dV = V_t - V_0$.

557    Tissue processing

558         Samples were fixed in 4% paraformaldehyde (PFA). For cryosectioning, samples were

559    incubated in the following series of solutions: 10% sucrose, 20% sucrose, 30% sucrose, 1:1

560    mixture of 30% sucrose and OCT (overnight), and OCT (1 hour). Samples were frozen in OCT.

561    Immunostaining

562         Cryosections were blocked and permeabilized (0.3% Triton-X-100 in PBS; 5% serum),

563    incubated in primary antibodies overnight and secondary antibodies for 2 hours. Sections were

564 counterstained with Hoechst 33342 (Invitrogen H3570, 1:10000) and mounted using

565 Fluoromount-G (SouthernBiotech). The following primary antibodies were used: chicken anti-

566 GFP (Abcam ab13970; 1:1000), mouse anti-Aqp1 (Santa Cruz sc-32737; 1:100), rabbit anti-

567 CHD4 (Abcam ab72418, 1:200), rabbit anti-NKCC1 (Abcam ab59791; 1:500), rat anti-HA

568 (Roche 11867423001; 1:1000). Secondary antibodies were selected from the Alexa series

569 (Invitrogen, 1:500). Images were acquired using Zeiss LSM880 confocal microscope with 20x

570 objective.

571 Co-IP

572 Tissues were homogenized in NET buffer (150mM NaCl, 10mM Tris 8.0, 5mM EDTA,

573 10% glycerol and 2% Triton-100) supplemented with protease inhibitors. Protein concentration

574 was determined by BCA assay (Thermo Scientific 23227). Lysates with same amount of total

575 protein (250-1000µg based on experiments) were pre-cleared at 4° C for 2hr with Protein G

576 agarose and then incubated with desired antibody or control antibody at 4° C overnight (no beads

577 present during antibody incubation). Protein G agarose beads were added to lysate-antibody

578 mixture after overnight incubation for 2hr. Beads were washed thoroughly and then eluted by

579 boiling in 2% SDS. ChP tissues were pooled across 7 litters of P0 pups and 30 adults to achieve

580 sufficient protein for Co-IP.

581 Immunoblotting

582 Tissues were homogenized in RIPA buffer supplemented with protease and phosphatase

583 inhibitors. Protein concentration was determined by BCA assay (Thermo Scientific 23227).

584 Samples were denatured in 2% SDS with 2-mercaptoethanol by heating at 37°C (for NKCC1) or

585 95°C (for CHD4 and other NuRD complex proteins) for 5 minutes. Equal amounts of proteins

586 were loaded and separated by electrophoresis in a 4-15% gradient polyacrylamide gel (BioRad

587   #1653320) or NuPAGE 4-12% Bis-Tris gel (Invitrogen #NP0322), transferred to a nitrocellulose

588   membrane (250mA, 1.5 hours, on ice), blocked in filtered 5% BSA or milk in TBST, incubated

589   with primary antibodies overnight at 4°C followed by HRP conjugated secondary antibodies

590   (1:5000) for 1 hour, and visualized with ECL substrate. For phosphorylated protein analysis, the

591   phospho-proteins were probed first, and then blots were stripped (Thermo Scientific 21059) and

592   reprobed for total proteins. For co-IP protein analysis, TrueBlot secondary antibody (eBioscience

593   18-8816-33) was used to detect only non-denatured IgG and avoid background signal from IP

594   antibody. The following primary antibodies were used: rabbit anti-NKCC1 (Abcam ab59791;

595   1:1000), rabbit anti-pNKCC1 (EMD Millipore ABS1004; 1:1000), rabbit anti-ATP1a1 (Upstate

596   C464.6/05-369; 1:250, goat-anti-klotho (R&D AF1819-sp; 1:200), rabbit anti-GAPDH (Sigma

597   G9545; 1:10000), mouse anti-HA (Abcam ab130275; 1:1000), rabbit anti-CHD4 (Abcam

598   ab72418; 1:2000), rabbit anti-MBD3 (Abcam ab157464; 1:1000), rabbit anti-HDAC1 (Abcam

599   ab7028; 1:2000), mouse anti-HDAC2 (Abcam 51832; 1:2000).

600   <u>Quantitative RT-PCR</u>

601   For mRNA expression analyses, the ChP were collected and pooled from 2 pups. RNA

602   was isolated using the MirVana miRNA isolation kit (Invitrogen AM1561) following

603   manufacturer's specifications without miRNA enrichment step. Extracted RNA was quantified

604   spectrophotometrically and 100ng was reverse-transcribed into cDNA using the High Capacity

605   cDNA Reverse Transcription kit (Applied Biosystems #4368814) following manufacturer's

606   specifications. RT-qPCRs were performed in duplicate using Taqman Gene Expression Assays

607   and Taqman Gene Expression Master Mix (Applied Biosystems) with GAPDH as an internal

608   control. Cycling was executed using the StepOnePlus Real-Time PCR System (Invitrogen) and

609   analysis of relative gene expression was performed using the $2^{-\Delta\Delta CT}$ method. Technical replicates

610     were averaged for their cycling thresholds and further calculations were performed with those

611     means.

612     *In utero* intracerebroventricular injection (ICV)

613     Timed pregnant mice (E14.5) were deeply anesthetized by isoflurane and placed on warm

614     pads. Laparotomy was performed and AAV solution was delivered into the lateral ventricle of

615     each embryo using glass capillary pipettes. The abdominal incision was then sutured. Meloxicam

616     analgesia was longitudinally delivered according to IACUC protocol.

617     Intraventricular kaolin injection in postnatal pups

618     Postnatal day 4 pups (P4) were deeply anesthetized by hypothermia. 1μl of sterile kaolin

619     solution (25% in PBS) was delivered into the left lateral ventricle using glass capillary pipettes.

620     The lateral ventricle location was determined as in between bregma and lambda, and 1mm from

621     mid-line. The pups were then warmed and returned to the dam.

622     AAV production

623     The original AAV-NKCC1 plasmid was purchased from Addgene (pcDNA3.1 HA CFP

624     hNKCC1 WT (NT15-H) was a gift from Biff Forbush: Addgene plasmid # 49077;

625     http://n2t.net/addgene:49077; RRID:Addgene_49077). The plasmid carries an 3xHA tag at the

626     N-terminal of NKCC1 to allow detection and separation from endogenous NKCC1. The CFP tag

627     was removed by BsaI digestion to reduce insert size for AAV production. Virus production and

628     purification were performed by the Penn Vector Core. Due to the very large size of the plasmid

629     we experienced variable infection efficiency. All mice receiving AAV-NKCC1 were analyzed

630     for HA expression after every experiment to confirm infection efficiency. AAV-GFP and AAV-

631     Cre were purchased from BCH viral core at Boston Children's Hospital.

Magnetic resonance imaging (MRI)

632

633    Mice were imaged using Bruker BioSpec small animal MRI (7T) at 2wk and P50 while

634    under anesthesia by isoflurane. A warm pad was used to maintain body temperature. Breathing

635    rate and heart rate were monitored to reflect the depth of anesthesia. All axial T2 images were

636    acquired using the following criteria: TE/TR=60/4000; Ave=8; RARE=4; slice thickness=0.6mm.

637    Ventricle volumes were calculated by manual segmentation using FIJI/ImageJ. In studies with

638    unilateral kaolin injection, 3D reconstruction of the ventricles was performed by manual

639    segmentation in ITK-SNAP (Madan, 2015) and exported through ParaView.

Constant rate CSF infusion test (ICP and compliance measurement)

640

641    An apparatus was developed to perform a constant infusion test in mice through a single

642    catheter for both infusion of CSF and monitoring of ICP. A 20cc syringe was filled with aCSF

643    and placed in an automated infusion pump (GenieTouch, Kent Scientific Co., Denver) and set to

644    deliver a constant rate infusion of 1-4 uL/minute. The syringe was connected via pressure tubing

645    to hemostasis valve Y connector (Qosina, NY). A fiberoptic ICP sensor (Fiso Technologies Inc,

646    Québec, Canada) was inserted through the other port of the rotating hemostat and then into 0.55

647    mm diameter catheter until the sensor was flush with the catheter's distal tip. The entire

648    apparatus and tubing was carefully screened to ensure the absence of air bubbles. Adult mice

649    were then deeply anesthetized, placed on a warm pad, and head-fixed with ear bars. The distal

650    end of the infusion device (catheter with fiberoptic sensor) was placed inside lateral ventricle (-

651    0.4mm (anterior-posterior) and 1.2mm (medial-lateral) with respect to Bregma, and a depth of 2

652    mm from the outer edge of the skull); the catheter was then sealed with Vetbond (3M,

653    Minnesota). Intraventricular access and water-tight seal was confirmed by observation of arterial

654    and respiratory waveforms in the ICP signal and a transient rise in ICP upon gentle compression

655    of the abdomen and thorax. Two minutes of baseline ICP were recorded before initiating the

656    infusion of aCSF. As the infusion proceeded, careful observation was made of the mouse's

657    respiratory rate. After the ICP level reached a new plateau, the infusion was discontinued. The

658    procedure was terminal. Parameters of the Marmarou model of CSF dynamics for constant rate

659    infusions were estimated by a non-linear least squares fit of the model to the ICP data (Czosnyka

660    et al., 2012)

$$ICP(t) = \frac{\left[i_{infusion} + \frac{ICP_{baseline} - p_0}{R_{CSF}}\right] \cdot [ICP_{baseline} - p_0]}{\frac{ICP_{baseline} - p_0}{R_{CSF}} + i_{infusion} \cdot \left[e^{-\frac{\left[i_{infusion} + \frac{ICP_{baseline} - p_0}{R_{CSF}}\right]}{C_i} t}\right]}$$

661    where $i_{infusion}$ is the rate of infusion, $ICP_{baseline}$ is the ICP level before infusion, $p_0$ is a pressure in

662    the storage arm of the model, $R_{CSF}$ is the resistance to CSF outflow, and $C_i$ is the compliance

663    coefficient.

## QUANTIFICATION AND STATISTICAL ANALYSIS

665    Biological replicates (N) were defined as samples from distinct individual animals,

666    analyzed either in the same experiment or within multiple experiments, with the exception when

667    individual animal could not provide sufficient sample (i.e. CSF), in which case multiple animals

668    were pooled into one biological replicate and the details are stated in the corresponding figure

669    legends. Statistical analyses were performed using Prism 7 or R. Outliers were excluded using

670    ROUT method (Q = 1%). Appropriate statistical tests were selected based on the distribution of

671    data, homogeneity of variances, and sample size. The majority of the analyses were done using

672    One-way ANOVA with multiple comparison correction (Sidak) or Welch's unpaired t-test,

673    except for Fig. 1E-G, and Fig. 1I-J where the analysis was done by Welch's ANOVA with

674    Dunnett's T3 multiple comparison test, and Fig. 1L where the analysis was done using

675    Kolmogorov-Smirnov test. F tests or Bartlett's tests were used to assess homogeneity of

676    variances between data sets. Parametric tests (t-test, ANOVA) were used only if data were

677    normally distributed and variances were approximately equal. Otherwise, nonparametric

678    alternatives were chosen. Data are presented as means ± standard deviation (SD). If multiple

679    measurements were taken from a single individual, data are presented as means ± standard errors

680    of the mean (SEMs). Please refer to figure legends for sample size. $p$ values < 0.05 were

681    considered significant (* $p < 0.05$, ** $p < 0.01$, *** $p < 0.001$, **** $p < 0.0001$). Exact p values

682    can be found in the figure legends. P values are also marked in the figures where space allows.

683

## REFERENCES:

Almagro Armenteros JJ, Tsirigos KD, Sonderby CK, Petersen TN, Winther O, Brunak S, von Heijne G, Nielsen H (2019) SignalP 5.0 improves signal peptide predictions using deep neural networks. *Nature biotechnology* 37:420-423.

Amin H, Marinaro F, De Pietri Tonelli D, Berdondini L (2017) Developmental excitatory-to-inhibitory GABA-polarity switch is disrupted in 22q11.2 deletion syndrome: a potential target for clinical therapeutics. *Scientific reports* 7:15752.

Anders S, Pyl PT, Huber W (2015) HTSeq--a Python framework to work with high-throughput sequencing data. *Bioinformatics* 31:166-169.

Antila S, Karaman S, Nurmi H, Airavaara M, Voutilainen MH, Mathivet T, Chilov D, Li Z, Koppinen T, Park JH, Fang S, Aspelund A, Saarma M, Eichmann A, Thomas JL, Alitalo K (2017) Development and plasticity of meningeal lymphatic vessels. *The Journal of experimental medicine* 214:3645-3667.

Aquilina K, Pople IK, Sacree J, Carter MR, Edwards RJ (2012) The constant flow ventricular infusion test: a simple and useful study in the diagnosis of third ventriculostomy failure. *Journal of neurosurgery* 116:445-452.

Banerjee A, Rikhye RV, Breton-Provencher V, Tang X, Li C, Li K, Runyan CA, Fu Z, Jaenisch R, Sur M (2016) Jointly reduced inhibition and excitation underlies circuit-wide changes in cortical processing in Rett syndrome. *Proceedings of the National Academy of Sciences of the United States of America* 113:E7287-E7296.

Bhargava P, Schnellmann RG (2017) Mitochondrial energetics in the kidney. *Nature reviews Nephrology* 13:629-646.

Cserr H (1965) Potassium exchange between cerebrospinal fluid, plasma, and brain. *The American journal of physiology* 209:1219-1226.

Czosnyka M, Czosnyka Z, Agarwal-Harding KJ, Pickard JD (2012) Modeling of CSF dynamics: legacy of Professor Anthony Marmarou. *Acta neurochirurgica Supplement* 113:9-14.

Damkier HH, Brown PD, Praetorius J (2013) Cerebrospinal fluid secretion by the choroid plexus. *Physiological reviews* 93:1847-1892.

Darman RB, Forbush B (2002) A regulatory locus of phosphorylation in the N terminus of the Na-K-Cl cotransporter, NKCC1. *The Journal of biological chemistry* 277:37542-37550.

Deidda G, Parrini M, Naskar S, Bozarth IF, Contestabile A, Cancedda L (2015) Reversing excitatory GABAAR signaling restores synaptic plasticity and memory in a mouse model of Down syndrome. *Nature medicine* 21:318-326.

Delpire E, Gagnon KB (2019) Elusive role of the Na-K-2Cl cotransporter in the choroid plexus. *American journal of physiology Cell physiology* 316:C522-C524.

Dobin A, Davis CA, Schlesinger F, Drenkow J, Zaleski C, Jha S, Batut P, Chaisson M, Gingeras TR (2013) STAR: ultrafast universal RNA-seq aligner. *Bioinformatics* 29:15-21.

Draghici S, Khatri P, Tarca AL, Amin K, Done A, Voichita C, Georgescu C, Romero R (2007) A systems biology approach for pathway level analysis. *Genome research* 17:1537-1545.

Eide PK (2018) The pathophysiology of chronic noncommunicating hydrocephalus: lessons from continuous intracranial pressure monitoring and ventricular infusion testing. *Journal of neurosurgery* 129:220-233.

Fame RM, Lehtinen MK (2020) Emergence and Developmental Roles of the Cerebrospinal Fluid System. *Developmental Cell* 52:261-275.

Fencl V, Miller TB, Pappenheimer JR (1966) Studies on the respiratory response to disturbances of acid-base balance, with deductions concerning the ionic composition of cerebral interstitial fluid. *The American journal of physiology* 210:459-472.

Furey CG, Choi J, Jin SC, Zeng X, Timberlake AT, Nelson-Williams C, Mansuri MS, Lu Q, Duran D, Panchagnula S, Allocco A, Karimy JK, Khanna A, Gaillard JR, DeSpenza T, Antwi P, Loring E, Butler WE, Smith ER, Warf BC, Strahle JM, Limbrick DD, Storm PB, Heuer G, Jackson EM, Iskandar BJ, Johnston JM, Tikhonova I, Castaldi C, Lopez-Giraldez F, Bjornson RD, Knight JR, Bilguvar K, Mane S, Alper SL, Haider S, Guclu B, Bayri Y, Sahin Y, Apuzzo MLJ, Duncan CC, DiLuna ML, Gunel M, Lifton RP, Kahle KT (2018) De Novo Mutation in Genes Regulating Neural Stem Cell Fate in Human Congenital Hydrocephalus. *Neuron* 99:302-314 e304.

Gato A, Alonso MI, Martin C, Carnicero E, Moro JA, De la Mano A, Fernandez JM, Lamus F, Desmond ME (2014) Embryonic cerebrospinal fluid in brain development: neural progenitor control. *Croatian medical journal* 55:299-305.

Gilmore JH, Kang C, Evans DD, Wolfe HM, Smith JK, Lieberman JA, Lin W, Hamer RM, Styner M, Gerig G (2010) Prenatal and neonatal brain structure and white matter maturation in children at high risk for schizophrenia. *The American journal of psychiatry* 167:1083-1091.

Goodman JV, Bonni A (2019) Regulation of neuronal connectivity in the mammalian brain by chromatin remodeling. *Current opinion in neurobiology* 59:59-68.

Haddad MR, Donsante A, Zerfas P, Kaler SG (2013) Fetal Brain-directed AAV Gene Therapy Results in Rapid, Robust, and Persistent Transduction of Mouse Choroid Plexus Epithelia. *Molecular therapy Nucleic acids* 2:e101.

Hamann S, Herrera-Perez JJ, Zeuthen T, Alvarez-Leefmans FJ (2010) Cotransport of water by the Na+-K+-2Cl(-) cotransporter NKCC1 in mammalian epithelial cells. *The Journal of physiology* 588:4089-4101.

He Q, Nomura T, Xu J, Contractor A (2014) The developmental switch in GABA polarity is delayed in fragile X mice. *The Journal of neuroscience : the official journal of the Society for Neuroscience* 34:446-450.

Heiman M, Schaefer A, Gong S, Peterson JD, Day M, Ramsey KE, Suarez-Farinas M, Schwarz C, Stephan DA, Surmeier DJ, Greengard P, Heintz N (2008) A translational profiling approach for the molecular characterization of CNS cell types. *Cell* 135:738-748.

Huang da W, Sherman BT, Lempicki RA (2009) Systematic and integrative analysis of large gene lists using DAVID bioinformatics resources. *Nature protocols* 4:44-57.

Hudry E, Dashkoff J, Roe AD, Takeda S, Koffie RM, Hashimoto T, Scheel M, Spires-Jones T, Arbel-Ornath M, Betensky R, Davidson BL, Hyman BT (2013) Gene transfer of human

764   Apoe isoforms results in differential modulation of amyloid deposition and neurotoxicity
765   in mouse brain. *Science translational medicine* 5:212ra161.

766   Hyde TM, Lipska BK, Ali T, Mathew SV, Law AJ, Metitiri OE, Straub RE, Ye T, Colantuoni C,
767   Herman MM, Bigelow LB, Weinberger DR, Kleinman JE (2011) Expression of GABA
768   signaling molecules KCC2, NKCC1, and GAD1 in cortical development and
769   schizophrenia. *The Journal of neuroscience : the official journal of the Society for*
770   *Neuroscience* 31:11088-11095.

771   Kahle KT, Kulkarni AV, Limbrick DD, Jr., Warf BC (2016) Hydrocephalus in children. *Lancet*
772   387:788-799.

773   Kaler SG (1994) Menkes disease. *Advances in pediatrics* 41:263-304.

774   Keep RF, Jones HC (1990) A morphometric study on the development of the lateral ventricle
775   choroid plexus, choroid plexus capillaries and ventricular ependyma in the rat. *Brain*
776   *research Developmental brain research* 56:47-53.

777   Lalou AD, Czosnyka M, Donnelly J, Pickard JD, FmedSci, Nabbanja E, Keong NC, Garnett M,
778   Czosnyka ZH (2018) Cerebral autoregulation, cerebrospinal fluid outflow resistance, and
779   outcome following cerebrospinal fluid diversion in normal pressure hydrocephalus.
780   *Journal of neurosurgery* 130:154-162.

781   Li Q, Aalling NN, Forstera B, Erturk A, Nedergaard M, Mollgard K, Xavier ALR (2020)
782   Aquaporin 1 and the Na(+)/K(+)/2Cl(-) cotransporter 1 are present in the leptomeningeal
783   vasculature of the adult rodent central nervous system. *Fluids and barriers of the CNS*
784   17:15.

785   Liddelow SA, Dziegielewska KM, Ek CJ, Habgood MD, Bauer H, Bauer HC, Lindsay H,
786   Wakefield MJ, Strazielle N, Kratzer I, Mollgard K, Ghersi-Egea JF, Saunders NR (2013)
787   Mechanisms that determine the internal environment of the developing brain: a
788   transcriptomic, functional and ultrastructural approach. *PloS one* 8:e65629.

789   LoTurco JJ, Owens DF, Heath MJ, Davis MB, Kriegstein AR (1995) GABA and glutamate
790   depolarize cortical progenitor cells and inhibit DNA synthesis. *Neuron* 15:1287-1298.

791   Love MI, Huber W, Anders S (2014) Moderated estimation of fold change and dispersion for
792   RNA-seq data with DESeq2. *Genome biology* 15:550.

793   Lun MP, Johnson MB, Broadbelt KG, Watanabe M, Kang YJ, Chau KF, Springel MW, Malesz
794   A, Sousa AM, Pletikos M, Adelita T, Calicchio ML, Zhang Y, Holtzman MJ, Lidov HG,
795   Sestan N, Steen H, Monuki ES, Lehtinen MK (2015) Spatially heterogeneous choroid
796   plexus transcriptomes encode positional identity and contribute to regional CSF
797   production. *The Journal of neuroscience : the official journal of the Society for*
798   *Neuroscience* 35:4903-4916.

799   Madan CR (2015) Creating 3D visualizations of MRI data: A brief guide. *F1000Research* 4:466.

800   Madry C, Kyrargyri V, Arancibia-Carcamo IL, Jolivet R, Kohsaka S, Bryan RM, Attwell D
801   (2018) Microglial Ramification, Surveillance, and Interleukin-1beta Release Are
802   Regulated by the Two-Pore Domain K(+) Channel THIK-1. *Neuron* 97:299-312 e296.

803   Milhorat TH, Mosher MB, Hammock MK, Murphy CF (1970) Evidence for choroid-plexus
804   absorption in hydrocephalus. *The New England journal of medicine* 283:286-289.

805 Munk AS, Wang W, Bechet NB, Eltanahy AM, Cheng AX, Sigurdsson B, Benraiss A, Mae MA,
806        Kress BT, Kelley DH, Betsholtz C, Mollgard K, Meissner A, Nedergaard M, Lundgaard I
807        (2019) PDGF-B Is Required for Development of the Glymphatic System. *Cell reports*
808        26:2955-2969 e2953.

809 Netsky MG, Shuangshoti S (1975) The choroid plexus in health and disease. Charlottesville:
810        University Press of Virginia.

811 Oreskovic D, Rados M, Klarica M (2017) Role of choroid plexus in cerebrospinal fluid
812        hydrodynamics. *Neuroscience* 354:69-87.

813 Owens DF, Liu X, Kriegstein AR (1999) Changing properties of GABA(A) receptor-mediated
814        signaling during early neocortical development. *Journal of neurophysiology* 82:570-583.

815 Pisella LI, Gaiarsa J-L, Diabira D, Zhang J, Khalilov I, Duan J, Kahle KT, Medina I (2019)
816        Impaired regulation of KCC2 phosphorylation leads to neuronal network dysfunction and
817        neurodevelopmental pathology. *Science Signaling* 12:eaay0300.

818 Rasmussen R, O'Donnell J, Ding F, Nedergaard M (2020) Interstitial ions: A key regulator of
819        state-dependent neural activity? *Progress in neurobiology* 193:101802.

820 Razzaque MS (2008) Klotho and Na+,K+-ATPase activity: solving the calcium metabolism
821        dilemma? *Nephrology, dialysis, transplantation : official publication of the European*
822        *Dialysis and Transplant Association - European Renal Association* 23:459-461.

823 Saunders NR, Dziegielewska KM, Møllgård K, Habgood MD (2018) Physiology and molecular
824        biology of barrier mechanisms in the fetal and neonatal brain. *The Journal of physiology*
825        596:5723-5756.

826 Schafer DP, Lehrman EK, Kautzman AG, Koyama R, Mardinly AR, Yamasaki R, Ransohoff
827        RM, Greenberg ME, Barres BA, Stevens B (2012) Microglia sculpt postnatal neural
828        circuits in an activity and complement-dependent manner. *Neuron* 74:691-705.

829 Schindelin J, Arganda-Carreras I, Frise E, Kaynig V, Longair M, Pietzsch T, Preibisch S,
830        Rueden C, Saalfeld S, Schmid B, Tinevez JY, White DJ, Hartenstein V, Eliceiri K,
831        Tomancak P, Cardona A (2012) Fiji: an open-source platform for biological-image
832        analysis. *Nature methods* 9:676-682.

833 Schneider CA, Rasband WS, Eliceiri KW (2012) NIH Image to ImageJ: 25 years of image
834        analysis. *Nature methods* 9:671-675.

835 Schuler MH, Lewandowska A, Caprio GD, Skillern W, Upadhyayula S, Kirchhausen T, Shaw
836        JM, Cunniff B (2017) Miro1-mediated mitochondrial positioning shapes intracellular
837        energy gradients required for cell migration. *Molecular biology of the cell* 28:2159-2169.

838 Shaolin Z, Zhanxiang W, Hao X, Feifei Z, Caiquan H, Donghan C, Jianfeng B, Feng L,
839        Shanghang S (2015) Hydrocephalus induced via intraventricular kaolin injection in adult
840        rats. *Folia neuropathologica* 53:60-68.

841 Shen MD, Kim SH, McKinstry RC, Gu H, Hazlett HC, Nordahl CW, Emerson RW, Shaw D,
842        Elison JT, Swanson MR, Fonov VS, Gerig G, Dager SR, Botteron KN, Paterson S,
843        Schultz RT, Evans AC, Estes AM, Zwaigenbaum L, Styner MA, Amaral DG, Piven J,
844        Hazlett HC, Chappell C, Dager S, Estes A, Shaw D, Botteron K, McKinstry R,
845        Constantino J, Pruett J, Schultz R, Zwaigenbaum L, Elison J, Evans AC, Collins DL,

846  Pike GB, Fonov V, Kostopoulos P, Das S, Gerig G, Styner M, Gu H, Piven J, Infant
847  Brain Imaging Study N (2017) Increased Extra-axial Cerebrospinal Fluid in High-Risk
848  Infants Who Later Develop Autism. *Biological psychiatry* 82:186-193.

849  Smith GM, Gallo G (2018) The role of mitochondria in axon development and regeneration.
850  *Developmental neurobiology* 78:221-237.

851  Somasekharan S, Monette MY, Forbush B (2013) Functional expression of human NKCC1 from
852  a synthetic cassette-based cDNA: introduction of extracellular epitope tags and removal
853  of cysteines. *PloS one* 8:e82060.

854  Sonnhammer ELL, Heijne Gv, Krogh A (1998) A hidden Markov model for predicting
855  transmembrane helices in protein sequences. In: In Proc of Sixth Int Conf on Intelligent
856  Systems for Molecular Biology (Glasgow, J. et al., eds), pp 175-182 Menlo Park, CA:
857  AAAI Press.

858  Sopjani M, Alesutan I, Dermaku-Sopjani M, Gu S, Zelenak C, Munoz C, Velic A, Foller M,
859  Rosenblatt KP, Kuro-o M, Lang F (2011) Regulation of the Na+/K+ ATPase by Klotho.
860  *FEBS letters* 585:1759-1764.

861  Spassky N, Merkle FT, Flames N, Tramontin AD, Garcia-Verdugo JM, Alvarez-Buylla A (2005)
862  Adult ependymal cells are postmitotic and are derived from radial glial cells during
863  embryogenesis. *The Journal of neuroscience : the official journal of the Society for
864  Neuroscience* 25:10-18.

865  Steen RG, Mull C, McClure R, Hamer RM, Lieberman JA (2006) Brain volume in first-episode
866  schizophrenia: systematic review and meta-analysis of magnetic resonance imaging
867  studies. *The British journal of psychiatry : the journal of mental science* 188:510-518.

868  Steffensen AB, Oernbo EK, Stoica A, Gerkau NJ, Barbuskaite D, Tritsaris K, Rose CR,
869  MacAulay N (2018) Cotransporter-mediated water transport underlying cerebrospinal
870  fluid formation. *Nature communications* 9:2167.

871  Trapnell C, Williams BA, Pertea G, Mortazavi A, Kwan G, van Baren MJ, Salzberg SL, Wold
872  BJ, Pachter L (2010) Transcript assembly and quantification by RNA-Seq reveals
873  unannotated transcripts and isoform switching during cell differentiation. *Nature
874  biotechnology* 28:511-515.

875  Vinchon M, Rekate H, Kulkarni AV (2012) Pediatric hydrocephalus outcomes: a review. *Fluids
876  and barriers of the CNS* 9:18.

877  Vinje V, Eklund A, Mardal KA, Rognes ME, Stoverud KH (2020) Intracranial pressure elevation
878  alters CSF clearance pathways. *Fluids and barriers of the CNS* 17:29.

879  Volpe JJ (2008) Neurology of the newborn. Philadelphia: Saunders/Elsevier.

880  Watanabe M, Zhang J, Mansuri MS, Duan J, Karimy JK, Delpire E, Alper SL, Lifton RP,
881  Fukuda A, Kahle KT (2019) Developmentally regulated KCC2 phosphorylation is
882  essential for dynamic GABA-mediated inhibition and survival. *Science Signaling*
883  12:eaaw9315.

884  Weiss K, Lazar HP, Kurolap A, Martinez AF, Paperna T, Cohen L, Smeland MF, Whalen S,
885  Heide S, Keren B, Terhal P, Irving M, Takaku M, Roberts JD, Petrovich RM, Schrier
886  Vergano SA, Kenney A, Hove H, DeChene E, Quinonez SC, Colin E, Ziegler A, Rumple

887     M, Jain M, Monteil D, Roeder ER, Nugent K, van Haeringen A, Gambello M, Santani A,
888     Medne L, Krock B, Skraban CM, Zackai EH, Dubbs HA, Smol T, Ghoumid J, Parker MJ,
889     Wright M, Turnpenny P, Clayton-Smith J, Metcalfe K, Kurumizaka H, Gelb BD, Baris
890     Feldman H, Campeau PM, Muenke M, Wade PA, Lachlan K (2020) The CHD4-related
891     syndrome: a comprehensive investigation of the clinical spectrum, genotype-phenotype
892     correlations, and molecular basis. *Genetics in medicine : official journal of the American*
893     *College of Medical Genetics* 22:389-397.

894     Williams CJ, Naito T, Arco PG, Seavitt JR, Cashman SM, De Souza B, Qi X, Keables P, Von
895     Andrian UH, Georgopoulos K (2004) The chromatin remodeler Mi-2beta is required for
896     CD4 expression and T cell development. *Immunity* 20:719-733.

897     Zeuthen T (1994) Cotransport of K+, Cl- and H2O by membrane proteins from choroid plexus
898     epithelium of Necturus maculosus. *The Journal of physiology* 478 ( Pt 2):203-219.

899     Zeuthen T, Macaulay N (2012) Cotransport of water by Na(+)-K(+)-2Cl(-) cotransporters
900     expressed in Xenopus oocytes: NKCC1 versus NKCC2. *The Journal of physiology*
901     590:1139-1154.

902     Zhang Y, Huang G, Shornick LP, Roswit WT, Shipley JM, Brody SL, Holtzman MJ (2007) A
903     transgenic FOXJ1-Cre system for gene inactivation in ciliated epithelial cells. *American*
904     *journal of respiratory cell and molecular biology* 36:515-519.

905

Figure 1

906
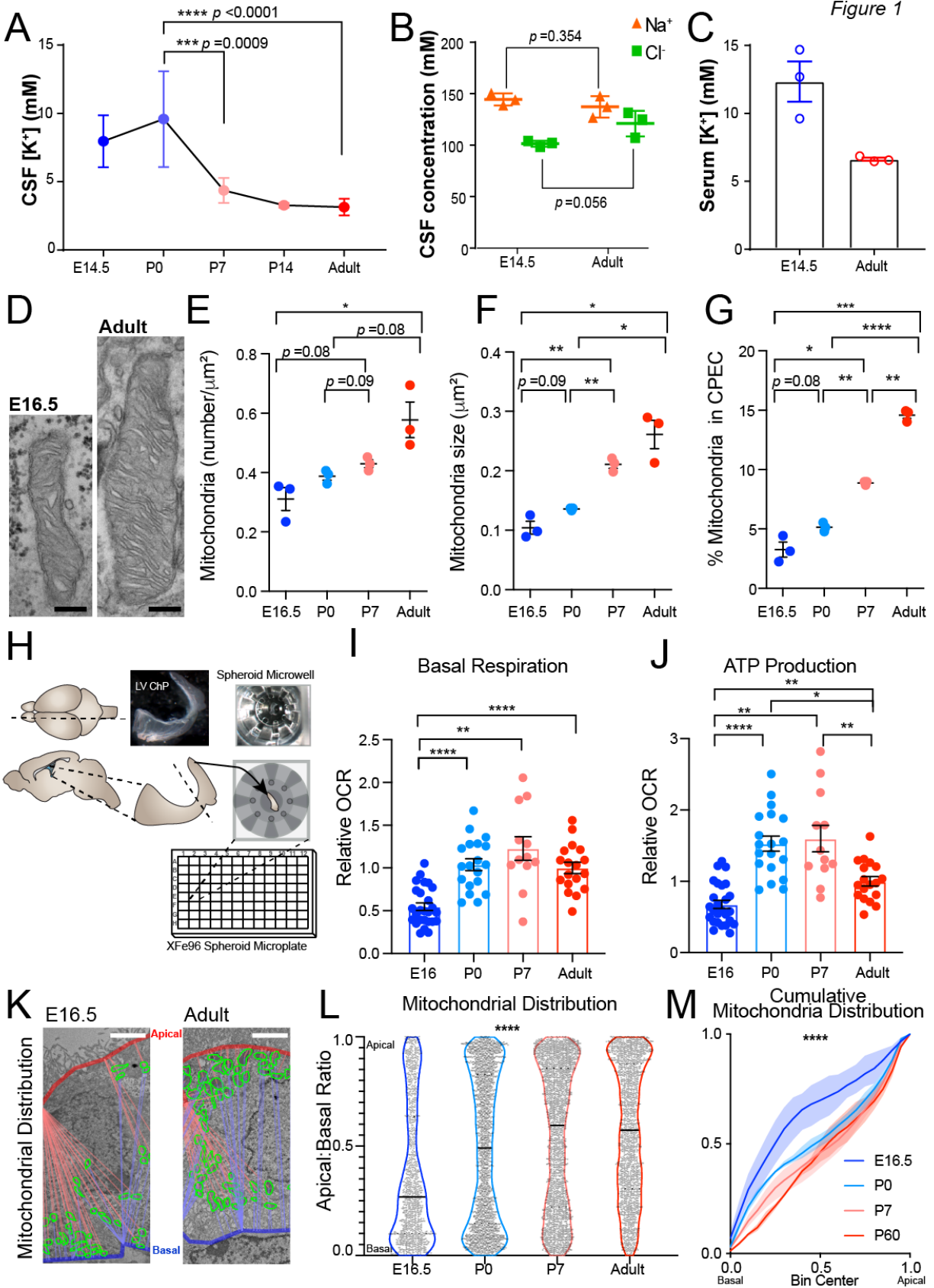
907 **Fig. 1. Postnatal CSF [K$^+$] decrease coincides with increased ChP metabolism. (A)** ICP-OES

908 quantification of CSF [K$^+$]. N = 6, **** $p < 0.0001$ by one-way ANOVA. Sidak's test was used

909 for P0 vs. P7 and P0 vs. adult comparison. *** $p = 0.0009$, **** $p < 0.0001$. **(B)** ICP-OES and

910 IC measurements of E14.5 and adult mouse CSF [Na$^+$] and [Cl$^-$]. N=3; Welch's t-test. **(C)** ICP-

911 OES measurements of embryo vs. adult mouse serum [K$^+$]. N=3. **(D)** Transmission micrographs

912 of mitochondria in LVChP. **(E-G)** Quantification of mitochondrial number (**E**), area (**F**), and %

913 area occupancy (**G**) in ChP epithelial cells. N =3 animals, 5-10 FOV per animal, *$p < 0.05$, **$p$

914 $< 0.01$, ***$p < 0.005$, ****$p < 0.001$; Welch's t-test. **(H)** Schematic of explant-based Agilent

915 Seahorse XFe96 test. **(I-J)** Oxidative respiration metrics over development. *$p < 0.05$, **$p <$

916 $0.01$, ****$p < 0.0001$; Welch's ANOVA with Dunnett's T3 multiple comparison test. **(K-L)**

917 Mitochondrial distribution between the apical and basal surfaces (Apical: Basal proximity ratio).

918 1 = apical surface. 0 = basal surface. Solid line indicates median and dashed line indicates

919 upper/lower quartiles. **** $p < 0.0001$; Kolmogorov–Smirnov test. **(M)** Cumulative distribution

920 of mitochondrial localization. Solid lines are the mean, shaded area represents the range. Scale

921 bar (d) = 250nm, (k) = 2μm. Unless otherwise noted, all quantitative data are presented as Mean

922 ± SEM.

923

Figure 2
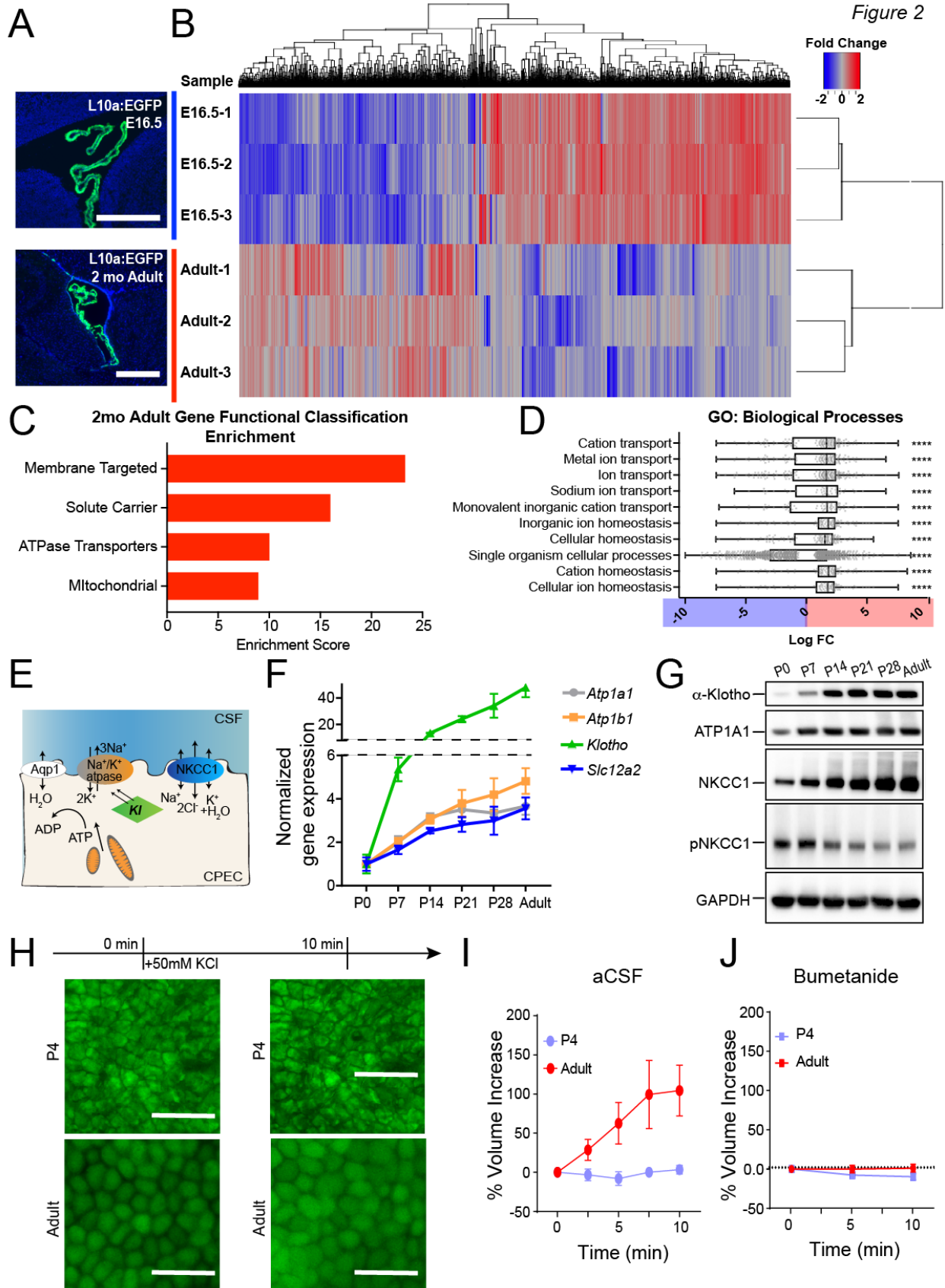
925    **Fig. 2. Choroid plexus epithelial cells display age-dependent translation of ion and water**

926    **transporters, in particular NKCC1. (A)** Rpl10a-conjugated EGFP expression in ChP epithelial

927    cells after *Foxj1*-Cre recombination in TRAP-BAC mice. **(B)** Heatmap and hierarchical

928    clustering of differentially expressed genes (adjusted p < 0.05). **(C)** Top 4 gene functional

929    clusters shown by DAVID to be enriched in Adult ChP epithelial cells over E16.5 ChP epithelial

930    cells. **(D)** Top 10 significantly enriched gene ontology (GO) terms for "Biological processes".

931    Plotted with boxes for quartiles and whiskers for $5^{th}$ and $95^{th}$ percentiles. The $\log_{10}$ fold change

932    (LogFC) is plotted for each expressed gene for the network. Positive values (red) indicate Adult

933    enrichment and negative values (blue) indicate E16.5 enrichment. *p* values are corrected for

934    multiple measures using Bonferroni correction. ***p* ≤0.01, ****p* ≤0.001, *****p* ≤0.0001. **(E)**

935    Schematics demonstrating the interaction of NKCC1, $Na^+/K^+$-ATPase, and Klotho on the apical

936    membrane of a ChP epithelial cell (CPEC). **(F-G)** RT-qPCR and immunoblotting of LVChP

937    during postnatal development. **(H)** Fluorescence images of Calcein-AM labeled epithelial cells

938    from LVChP explants under high extracellular $K^+$ challenge. Scale bar = 50μm. **(I-J)**

939    Quantification of ChP epithelia cellular volume by IMARIS 3D analysis. Percent volume

940    increase = $dV/V_0$ for each timepoint (t). $V_0$ = initial volume of the cell; t = subsequent timepoint

941    after addition of challenge; $dV = V_t - V_0$ x 100%. At least 10 cells were analyzed for each explant

942    from one animal; N = 4.

Figure 3
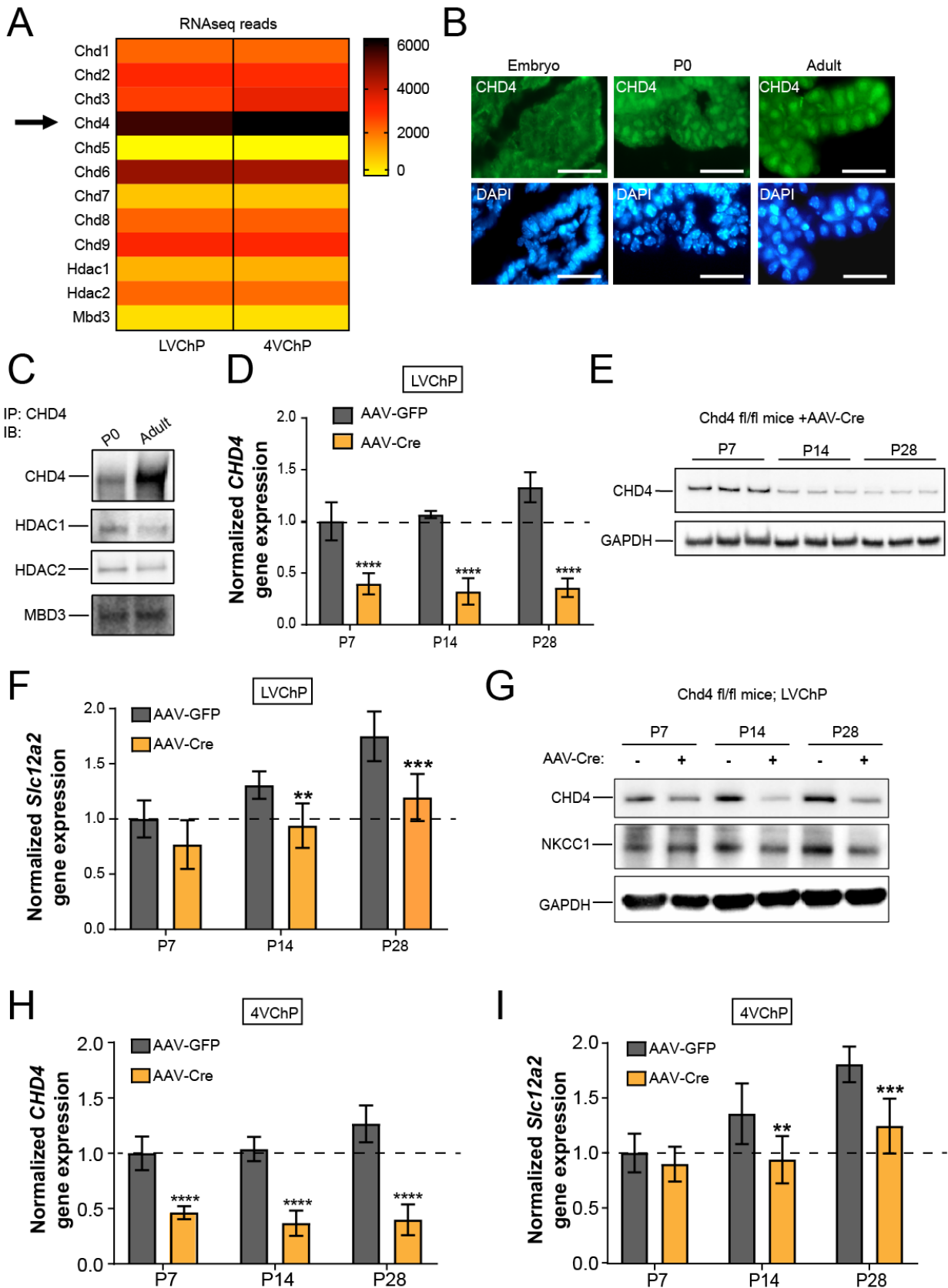
944     **Fig. 3. NKCC1 temporal expression requires CHD4/NuRD complex. (A)** RNAseq data

945     showing expression of CHD and other NuRD units by the ChP. **(B)** Immunofluorescence images

946     of CHD4 in the ChP epithelia at E16.5, P0, and adult; Scale bar = 30μm. **(C)** Immunoblots of

947     Co-IP by CHD4 antibody. **(D)** RT-qPCR of CHD4 transcripts in ChP with AAV2/5-Cre

948     infection.**** *p*< 0.0001, N = 7, Welch's t-test. **(E)** Immunoblot of CHD4 in AAV-cre mice

949     ChP lysate with. **(F)** RT-qPCR of NKCC1 expression in AAV-cre vs. AAV-GFP mice ChP. All

950     values were normalized to P7 AAV-GFP control mice. ***p* = 0.0015, ****p* < 0.001, N = 7,

951     Welch's t-test. **(G)** Immunoblot of NKCC1 in LVChP lysates from AAV-cre vs. AAV-GFP mice.

952     **(H-I)** CHD4 and NKCC1 RT-qPCR in 4VChP. ** p = 0.0083, *** *p* < 0.001, **** *p* < 0.0001,

953     N = 7, Welch's t-test.

954

*Figure 4*



955
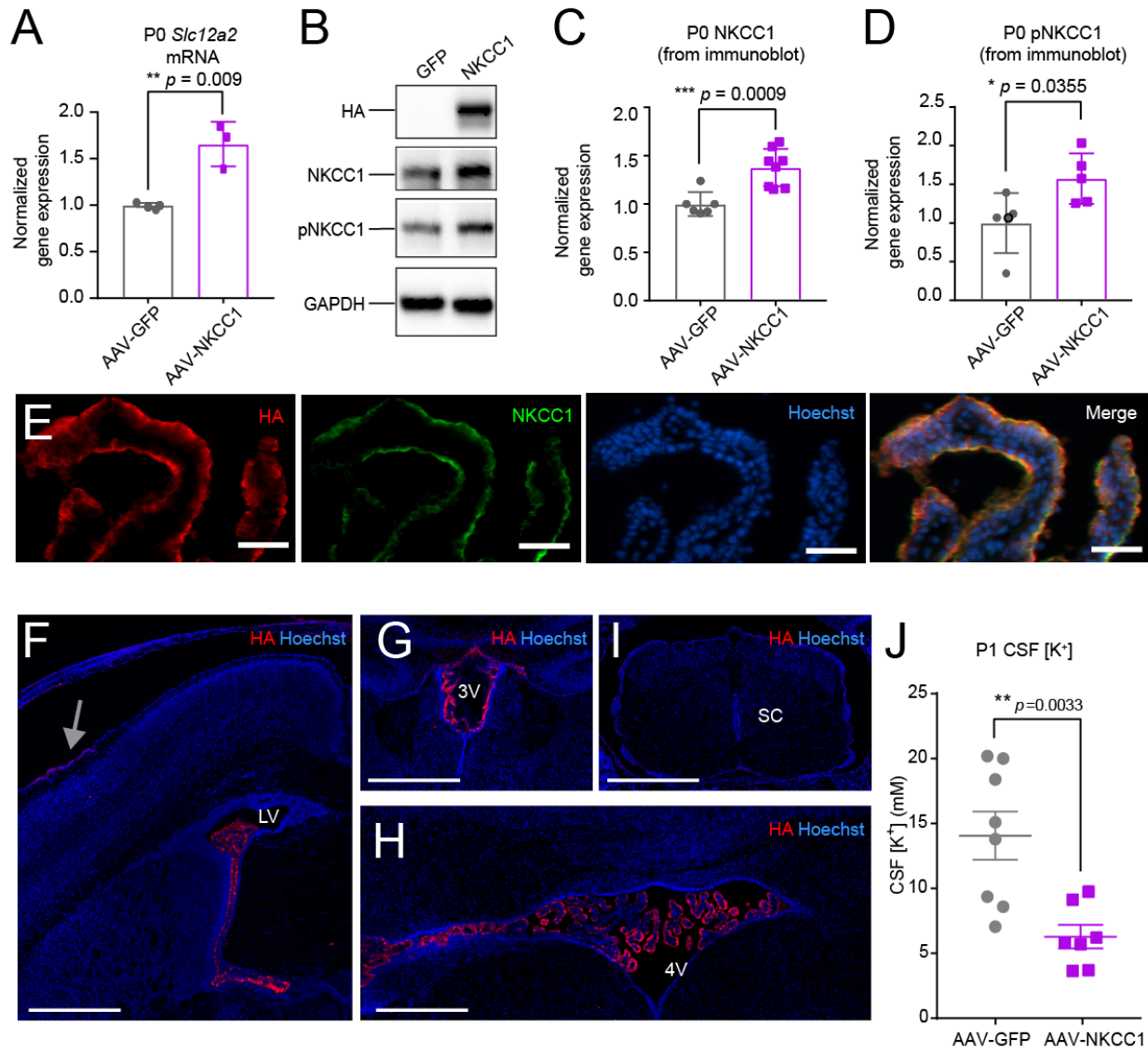
956 **Fig. 4. ChP NKCC1 actively mediates CSF K$^+$ clearance in the first postnatal week. (A)** RT-

957 qPCR of NKCC1 mRNA levels in P0 mice. ** $p$ = 0.009, N=3; Welch's t-test. **(B)** Immunoblots

958 from AAV-NKCC1 vs. AAV-GFP P0 mice ChP lysates. **(C-D)** Quantification of all

959 immunoblots of NKCC1 **(C)** *** $p$ = 0.0009, N=7; Welch's t-test; and pNKCC1 **(D)** * $p$ =

960 0.0355, N=5; Welch's t-test. **(E)** Immunofluorescence images showing co-localization of 3xHA

961 tag and NKCC1 in P0 ChP. Scale bar = 50μm. **(F-I)** Immunofluorescence images of HA in

962 AAV2/5-NKCC1 transduced brain at P1: the LVChP **(F)**, 3$^{rd}$ ventricle ChP (3VChP; **G**), 4VChP

963 **(H)**, and the spinal cord (**I**; sc = spinal cord). Traces of HA is shown in the meninges near the

964 injection site (grey arrow). Scale bar = 500μm. **(J)** ICP-OES measurements of CSF [K$^+$] from

965 AAV-NKCC1 vs. AAV-GFP P1 mice (N = 8 in AAV-GFP cohort; N = 7 in AAV-NKCC1

966 cohort). ** $p$ = 0.0033; Welch' t-test.

967

968

969

Figure 5



970
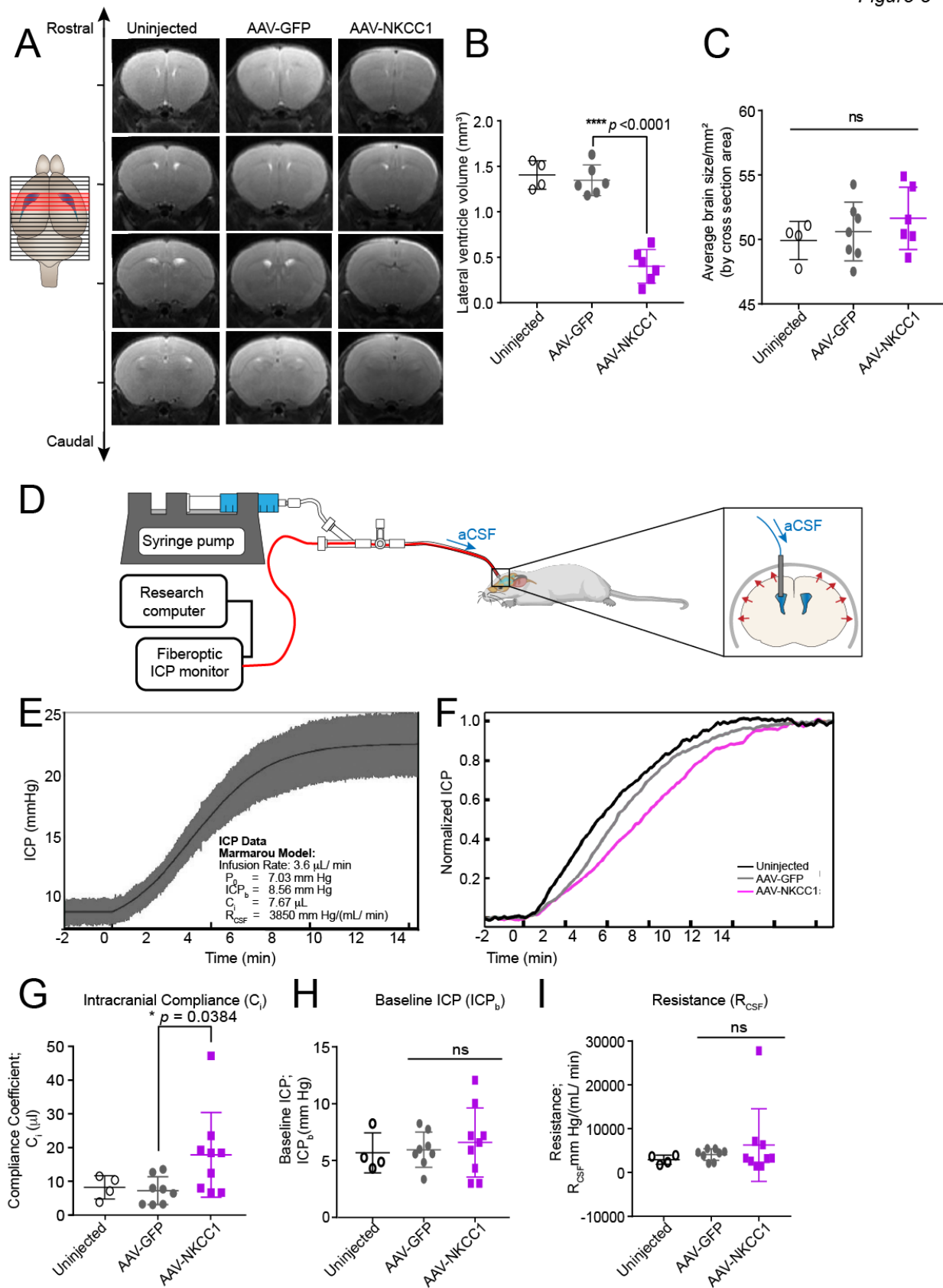
971 **Fig. 5. ChP NKCC1 overexpression reduces brain ventricular volume and increases**

972 **intracranial compliance. (A)** T2-weighted live MRI images. Only slices with visible LV are

973 shown (marked red in the schematics). **(B)** LV volumes. Uninjected N = 4; AAV-GFP and AAV-

974 NKCC1 N = 6; ****$p$ < 0.0001; Welch's t-test. **(C)** Brain sizes, which are presented as the

975 average coronal section area from all images with visible ventricles (NKCC1 OE data were

976 calculated using the matching images to the controls, regardless of ventricles visibility).

977 Uninjected N = 4; AAV-GFP and AAV-NKCC1 N = 6; Welch's t-test. **(D)** Schematic of *in vivo*

978 constant rate CSF infusion test. **(E)** Example of ICP curve during the infusion test (infusion

979 begins at 0 min) in an AAV-GFP mouse, fitted to Marmarou's model. Values extracted include:

980 baseline ICP ($ICP_b$), a pressure-independent compliance coefficient ($C_i$) and the resistance to

981 CSF outflow ($R_{CSF}$). **(F)** Example ICP recordings from AAV-NKCC1 mice and controls. For

982 clarity, data have been low pass filtered to remove the waveform components. **(G)** Compliance

983 coefficients. Uninjected N = 4; AAV-GFP N = 8; AAV-NKCC1 N = 9; *$p$ = 0.0384; Welch's t-

984 test. **(H-I)** Plots of baseline ICP and resistance to CSF outflow ($R_{CSF}$) at 5-7 weeks. Uninjected

985 N=4, AAV-GFP N=8, AAV-NKCC1 N=9; Welch's t-test.

986

Figure 6
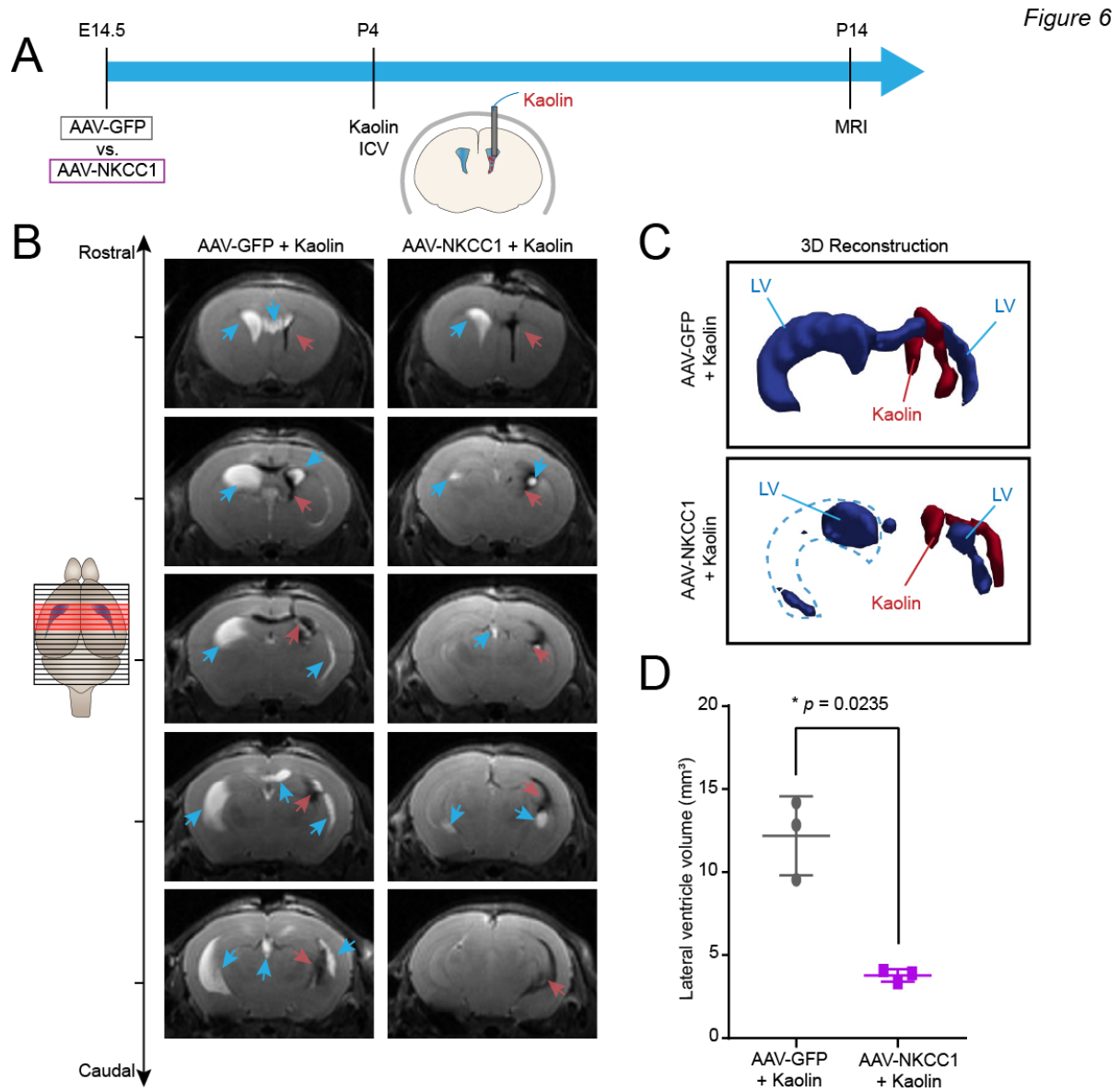
988  **Fig. 6. ChP NKCC1 overexpression mitigates ventriculomegaly in an obstructive**

989  **hydrocephalus model. (A)** Schematics showing the workflow: E14.5 in utero ICV of AAV2/5-

990  NKCC1 or AAV2/5-GFP, followed by ICV of kaolin at P4, and MRI at P14. **(B)** Representative

991  sequential brain images (rostral to caudal) by T2-weighted live MRI images. Blue arrows: LV.

992  Red arrows: kaolin. **(C)** 3D reconstruction of the LV and kaolin deposition. LV: blue. Kaolin:

993  red. **(D)** LV volumes. N = 3; *$p$ = 0.0.0235; Welch's t-test.

*Figure 7*
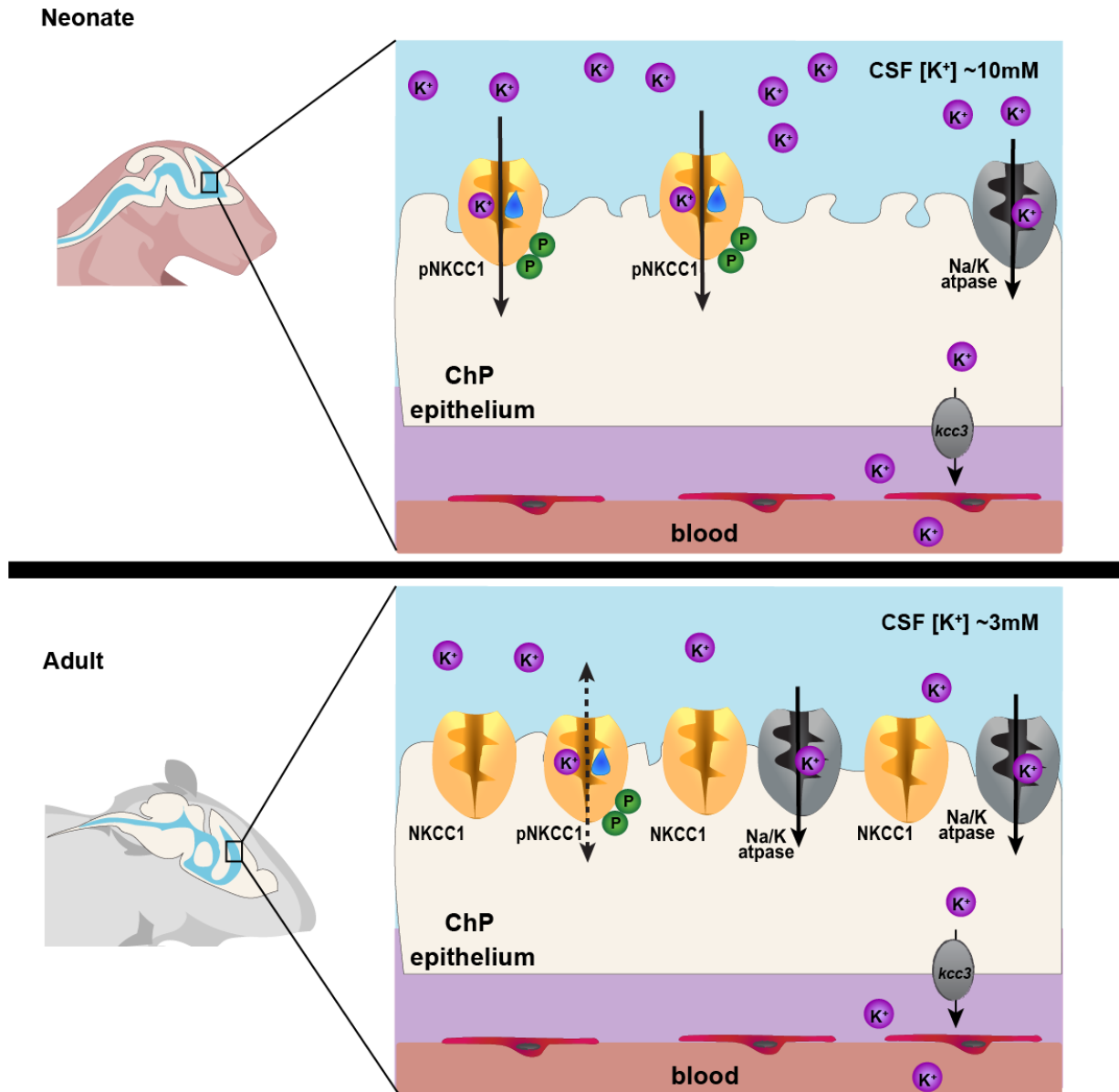
995  **Fig. 7. Working model of ChP NKCC1 mediating K$^+$-driven CSF outflow.** The schematics

996  describes ChP NKCC1 mediated K$^+$ and water clearance from CSF in neonatal mice, in

997  comparison to the adult scenario. For simplicity and clarity, only K$^+$ is depicted among all ions

998  and only NKCC1 and Na$^+$/K$^+$-ATPase are included. Neonatal (P0-7, left) ChP has high pNKCC1

999  than adult, albeit lower total NKCC1. Neonate CSF [K$^+$] is 2-3 fold higher than adult. With

1000  similar [Na$^+$] and [Cl$^-$], this [K$^+$] difference is sufficient to alter the total Nernst potential of

1001  epithelial cells and bias NKCC1 transport of K$^+$, together with water, out of CSF into the ChP in

1002  neonates.

1003